



CHALMERS
UNIVERSITY OF TECHNOLOGY

Synergistic radar and sub-millimeter radiometer retrievals of ice hydrometeors in mid-latitude frontal cloud systems

Downloaded from: <https://research.chalmers.se>, 2024-03-20 09:40 UTC

Citation for the original published paper (version of record):

Pfreundschuh, S., Fox, S., Eriksson, P. et al (2022). Synergistic radar and sub-millimeter radiometer retrievals of ice hydrometeors in mid-latitude frontal cloud systems. *Atmospheric Measurement Techniques*, 15(3): 677-699.
<http://dx.doi.org/10.5194/amt-15-677-2022>

N.B. When citing this work, cite the original published paper.



Synergistic radar and sub-millimeter radiometer retrievals of ice hydrometeors in mid-latitude frontal cloud systems

Simon Pfreundschuh¹, Stuart Fox², Patrick Eriksson¹, David Duncan³, Stefan A. Buehler⁴, Manfred Brath⁴, Richard Cotton², and Florian Ewald⁵

¹Department of Space, Earth and Environment, Chalmers University of Technology, 41296 Gothenburg, Sweden

²Met Office, FitzRoy Road, Exeter, EX1 3PB, United Kingdom

³ECMWF, Shinfield Park, Reading, RG2 9AX, United Kingdom

⁴Meteorologisches Institut, Fachbereich Geowissenschaften, Centrum für Erdsystem und Nachhaltigkeitsforschung (CEN), Universität Hamburg, Bundesstraße 55, 20146 Hamburg, Germany

⁵Institut für Physik der Atmosphäre, Deutsches Zentrum für Luft- und Raumfahrt, Pfaffenhofen, Germany

Correspondence: Simon Pfreundschuh (simon.pfreundschuh@chalmers.se)

Received: 29 September 2021 – Discussion started: 20 October 2021

Revised: 22 December 2021 – Accepted: 25 December 2021 – Published: 9 February 2022

Abstract. Accurate measurements of ice hydrometeors are required to improve the representation of clouds and precipitation in weather and climate models. In this study, a newly developed, synergistic retrieval algorithm that combines radar with passive millimeter and sub-millimeter observations is applied to observations of three frontally generated, mid-latitude cloud systems in order to validate the retrieval and assess its capabilities to constrain the properties of ice hydrometeors. To account for uncertainty in the assumed shapes of ice particles, the retrieval is run multiple times while the shape is varied. Good agreement with in situ measurements of ice water content and particle concentrations for particle maximum diameters larger than 200 μm is found for one of the flights for the large plate aggregate and the six-bullet rosette shapes. The variational retrieval fits the observations well, although small systematic deviations are observed for some of the sub-millimeter channels pointing towards issues with the sensor calibration or the modeling of gas absorption. For one of the flights the quality of the fit to the observations exhibits a weak dependency on the assumed ice particle shape, indicating that the employed combination of observations may provide limited information on the shape of ice particles in the observed clouds. Compared to a radar-only retrieval, the results show an improved sensitivity of the synergistic retrieval to the microphysical properties of ice hydrometeors at the base of the cloud.

Our findings indicate that the synergy between active and passive microwave observations may improve remote-sensing measurements of ice hydrometeors and thus help to reduce uncertainties that affect currently available data products. Due to the increased sensitivity to their microphysical properties, the retrieval may also be a valuable tool to study ice hydrometeors in field campaigns. The good fits obtained to the observations increase confidence in the modeling of clouds in the Atmospheric Radiative Transfer Simulator and the corresponding single scattering database, which were used to implement the retrieval forward model. Our results demonstrate the suitability of these tools to produce realistic simulations for upcoming sub-millimeter sensors such as the Ice Cloud Image or the Arctic Weather Satellite.

1 Introduction

The representation of clouds in climate models remains an important issue that causes significant uncertainties in their predictions (Zelinka et al., 2020). Improving and validating these models requires measurements that accurately characterize the distribution of hydrometeors in the atmosphere. At regional and global scales, such observations can be obtained efficiently only through remote sensing. Unfortunately, currently available remote-sensing observations do not constrain

the distribution of ice in the atmosphere well (Waliser et al., 2009; Eliasson et al., 2011; Duncan and Eriksson, 2018).

To address this, the Ice Cloud Imager (ICI) radiometer, to be launched on board the second generation of European operational meteorological satellites (MetOp-SG), will be the first operational sensor to provide global observations of clouds at microwave frequencies exceeding 183 GHz. Compared to microwave observations at currently available frequencies (≤ 183 GHz), observations at and above 243 GHz have been shown to be sensitive to a broader size range of hydrometeors (Buehler et al., 2012) as well as their shape and particle size distribution (Evans et al., 1998). Although the increased sensitivity to smaller particles and their microphysical properties is expected to help improve measurements of ice in the atmosphere, it also increases the complexity of simulations of cloud observations, which are an essential tool for performing these measurements in the first place.

In Pfreundschuh et al. (2020), we have developed a cloud-ice retrieval based on radar and passive sub-millimeter observations to investigate the potential benefits of a synergistic radar mission to fly in constellation with ICI on MetOp-SG. The simulation-based results from Pfreundschuh et al. (2020) indicate that combining active and passive observations across millimeter and sub-millimeter observations can indeed help to better constrain the distributions of ice hydrometeors in cloud retrievals. The principal aim of this study is to validate the synergistic retrieval using real observations and to investigate its ability to retrieve the vertical distributions of ice hydrometeors.

Since the retrieval has been shown to work on simulated observations, the validation of the synergistic retrieval essentially amounts to verifying the physical realism of the underlying forward model. The observations from the three flights considered here thus also constitute an opportunity to validate the radiative transfer model that is used in the retrieval, i.e., the Atmospheric Radiative Transfer Simulator (ARTS, Buehler et al., 2018) and the corresponding ARTS single scattering database (ARTS SSDB, Eriksson et al., 2018), to accurately simulate cloud observations at sub-millimeter wavelengths. Such simulations are of paramount importance not only for future cloud retrievals from ICI observations (Eriksson et al., 2020) but also for assimilating cloud-contaminated observations in numerical weather prediction models (Geer et al., 2017).

In this study, the synergistic retrieval is applied to co-located radar and microwave radiometer observations of three mid-latitude cloud systems. The sensitivity of the retrieval to the ice particle shape that is assumed in the forward simulations is tested by running the retrieval multiple times while varying the assumed shape. To test the accuracy of the retrieval, retrieval results are compared to in situ measurements of bulk ice water content (IWC) and particle size distributions (PSDs) for the two flights where these were available. Finally, we assess the consistency of the forward model simulations by investigating the agreement between

simulated and real observations as well as between retrieved atmospheric state and in situ measurements.

The remainder of this article is structured as follows: Sect. 2 provides a description of the datasets and the retrieval algorithm upon which this study is based. Section 3 presents the results of the retrieval as well as the comparisons to in situ data followed by a discussion of those results in Sect. 4 and conclusions in Sect. 5.

2 Data and methods

The synergistic retrieval algorithm uses combined observations from radar and passive microwave sensors to retrieve vertical profiles ice hydrometeor distributions. The passive observations for this study are taken from the MARSS (McGrath and Hewison, 2001) and ISMAR (Fox et al., 2017) radiometers on board the UK's BAe-146-301 Atmospheric Research Aircraft (FAAM BAe-146) aircraft. Since the instrumentation of the FAAM BAe-146 aircraft does not include a cloud radar, only flights for which the radiometer observations can be co-located with radar observations from another platform are suitable for the combined retrieval. Since ISMAR is currently the only operational radiometer with channels up to 664 and 874 GHz, the flights considered in this study provide a rare opportunity to study the synergies between radar and passive (sub-)millimeter observations using real observations.

An overview of the three flights and the corresponding meteorological contexts is provided in Fig. 1. The first considered flight, designated B984, was performed on 14 October 2016 as part of the North Atlantic Waveguide and Downstream Impact Experiment (NAWDEX), which took place during September and October 2016 (Schäfler et al., 2018). During this flight, a cloud system generated by an occluded front has been observed quasi-simultaneously by three research aircraft: The High Altitude and Long Range Research Aircraft (HALO, Krautstrunk and Giez, 2012), the FAAM BAe-146 and the Falcon 20 of the Service des Avions Français Instrumentations pour la Recherche en Environnement (SAFIRE). The two other flights, designated C159 and C161, were part of the PIKNMIX-F campaign, which took place in March 2019. These two flights were performed following the ground track of simultaneous overpasses of the CloudSat satellite. The observations probe clouds in different regions of a frontal system generated by a low-pressure system passing over Iceland around 21 March 2019. The cloud system observed during flight C159 is a stratiform, lightly precipitating cloud located in the warm sector of the frontal system, whereas the clouds observed during flight C161 are of convective origin and located in the active region of the cold front. All datasets that were used in this study are listed together with their sources in Table 1.

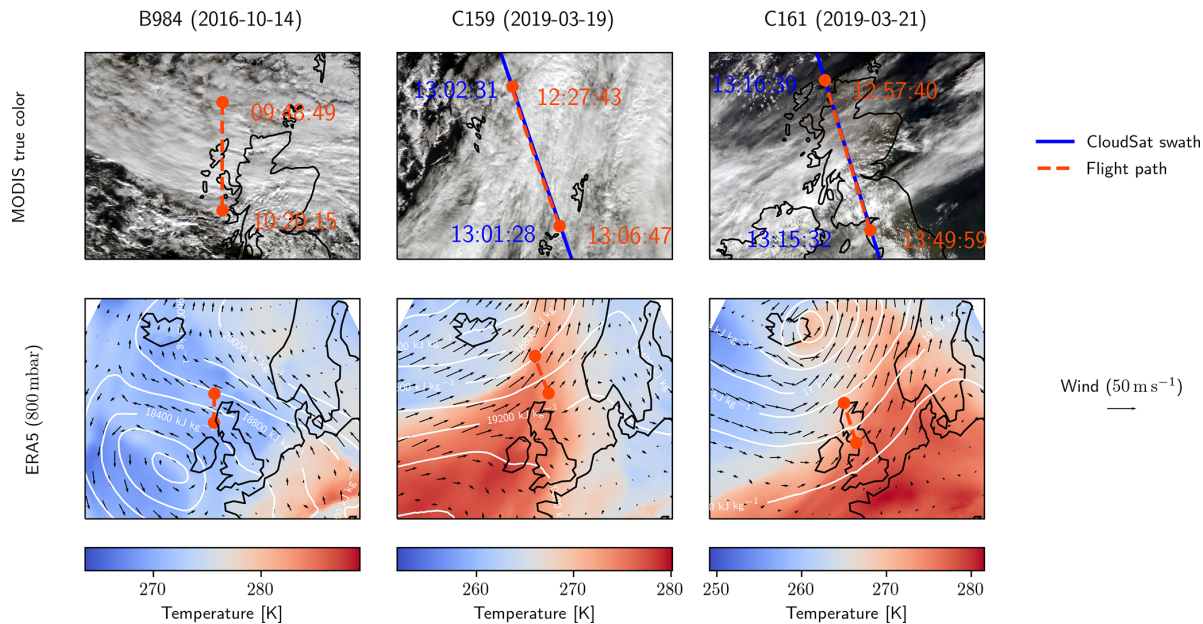


Figure 1. Flight paths of the cloud overpasses considered in this study. First row of panels shows the true-color composite derived from the closest overpasses of the MODIS (MCST, 2017) sensor on board the Aqua satellite. Second row shows ERA5 temperature (colored background), geopotential (contours) and wind speed (arrows) at the 800 mb pressure level from Hersbach et al. (2018).

Table 1. Datasets used in the this study.

Title	Usage	Reference
HALO Microwave Package measurements during North Atlantic Waveguide and Downstream impact EXperiment (NAWDEX)	Radar observations for flight B984	Konow et al. (2018), https://doi.org/10.1594/WDCC/HALO_measurements_4
CloudSat 1B-CPR	Radar observations for flight C159 (Granule 67658), C161 (Granule 68702)	Tanelli et al. (2008), CloudSat DPC (2021), https://www.cloudsat.cira.colostate.edu/data-products/1b-cpr (last access: 1 February 2022)
FAAM B984 ISMAR and T-NAWDEX flight: airborne atmospheric measurements from core instrument suite on board the BAE-146 aircraft	Radiometer observations and in situ measurements for flight B984	Facility for Airborne Atmospheric Measurements (2016), https://catalogue.ceda.ac.uk/uuid/46ca2a2cc8ce497fbf06beaf31f67098 (last access: 1 February 2022)
FAAM C159 PIKNMIX-F flight: airborne atmospheric measurements from core and non-core instrument suites on board the BAE-146 aircraft	Radiometer observations and in situ measurements for flight C159	Facility for Airborne Atmospheric Measurements (2019a), https://catalogue.ceda.ac.uk/uuid/68cfc7f294554646803c80b2a389e105 (last access: 1 February 2022)
FAAM C161 PIKNMIX-F flight: airborne atmospheric measurements from core and non-core instrument suites on board the BAE-146 aircraft	Radiometer observations for flight C159	Facility for Airborne Atmospheric Measurements (2019b), https://catalogue.ceda.ac.uk/uuid/133e15c47c024aa4b30e3f6f54af8b77 (last access: 1 February 2022)
ERA5 global reanalysis	A priori state and atmospheric background fields	Hersbach et al. (2018), https://doi.org/10.24381/cds.adbb2d47

2.1 Radar observations

The radar observations from the three flights are displayed in Fig. 2. Observations for flight B984 stem from the HAMP MIRA radar (Mech et al., 2014) on board the HALO aircraft, which operates at a frequency of 35 GHz and has been characterized and calibrated by Ewald et al. (2019). Its observations have been downsampled to a vertical resolution of 210 m and a horizontal resolution of roughly 700 m in order to reduce the computational complexity of the retrieval and to better match the field of view of the passive observations, which, at an altitude of 5 km, vary between about 900 m for the low-frequency channels and 200 m for the high-frequency channels.

The radar observations for flights C159 and C161 stem from the CloudSat Cloud Profiling Radar (CPR, Tanelli et al., 2008), which operates at 94 GHz. Since the CloudSat observations were affected strongly by ground clutter, the first five bins located completely above surface altitude were set to the reflectivity found in the sixth bin above the surface. The CPR observations have a vertical resolution of 240 m and a horizontal resolution of about 1.4 km. The horizontal distance between subsequent observations is 1.1 km.

While the radar observations for flight B984 come from an airborne radar, the observations for flights C159 and C161 stem from a spaceborne sensor. The high velocity of the spaceborne sensor causes significant temporal delay between co-located observations from the radiometers and the radar. Figure 3 displays the delay between co-located radar and radiometer observations with respect to the along-track distance for the three flight scenes. While the delays for flight B984 remain mostly within 5 min, they reach values exceeding 30 min for the two other flights.

2.1.1 MARSS

The MARSS radiometer measures microwave radiances at 89, 157 GHz and channels located around the water vapor line at 183 GHz. Although MARSS is a scanning radiometer only observations within 5° off nadir are used in the retrieval. The observations from the three flights are displayed in Fig. 4. Observations from channels that are sensitive to surface emission (89 and 157 GHz) are excluded from the retrieval for flight sections over land. The MARSS observations were mapped to the radar observations using nearest-neighbor interpolation.

2.1.2 ISMAR

The ISMAR radiometer has channels covering the frequency range from 118 up to 874 GHz. As for MARSS, only observations within 5° off nadir are used in the retrieval. The observations from the three flights are displayed in Fig. 5. Similar to for the two low-frequency channels of MARSS, the four outermost channels around the 118 GHz oxygen line

are not used over land. The matching of ISMAR observations to radar observations is performed in the same way as for MARSS. It should be noted that not all channels were available on all flights: the channels around 448 GHz were not available on the B984 flight, while two of the channels around 325 GHz were missing for the C159 and C161 flights. From the channels at 874 GHz only the *V* polarization was available for flights C159 and C161.

The polarized measurements at 243 and at 664 GHz for flight B984 were replaced by the average of the measured *H* and *V* polarizations. For flights C159 and C161, only the horizontally polarized measurements at 664 GHz were used due to excessive noise in the *V* channel.

2.2 In situ measurements

The in situ measurements that are relevant to this study are measurements of bulk ice water content using a Nevzorov hot-wire probe (Korolev et al., 2013) and PSDs recorded using DMT CIP-15 and CIP-100 probes, which measure size-resolved particle concentrations with resolutions of 15 and 100 µm, respectively. In situ measurements are available only for flights B984 and C159, which each consist of two parts: a high-level run during which the aircraft flew above the cloud system to perform the remote-sensing observations and a low-level run during which the aircraft flew at lower altitude through the cloud to perform the in situ measurements. A detailed view of the high- and low-level runs for the two flights is provided in Fig. 6. For flight C159, this view reveals a noticeable horizontal offset of 3 to 4 km between the ground tracks of radar and radiometer observations. Even larger deviations occur between certain parts of the low-level run and the ground tracks of the remote-sensing observations.

An overview of the measured IWC and PSDs is provided in Fig. 7. While for flight B984 the measured IWC is mostly consistent with the radar observations, there are clear disparities between the measured IWC and the CPR reflectivities for flight C159. This indicates that there may be considerable differences between the regions of the cloud that were sampled during the in situ sampling and the part that was observed by the CloudSat CPR.

The PSD profiles for flight B984 show a clear size-sorting pattern with a gradual decrease in the concentration of particles smaller than 200 µm and a simultaneous increase in the concentration of larger particles. For flight C159, high concentrations of small particles are encountered at low altitudes which decrease with altitude. For larger particles no systematic variation with altitude is observed.

2.3 Retrieval algorithm

The synergistic retrieval algorithm used in this study is based on the optimal estimation framework (Rodgers, 2000) and retrieves distributions of frozen and liquid hydrometeors together with water vapor by simultaneously fitting a forward

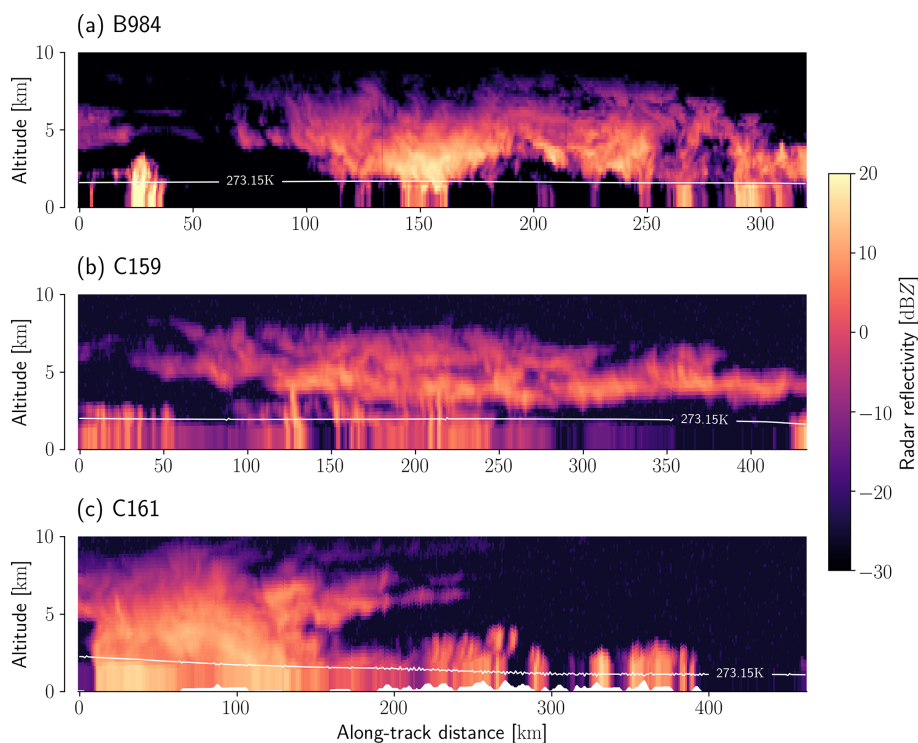


Figure 2. Radar observations from the flights used in this study. Panel (a) shows the radar reflectivity measured by the HAMP MIRA 35 GHz cloud radar. Panels (b) and (c) show the reflectivity measured by the CloudSat CPR at 94 GHz. The white line displays the ERA5 freezing level from Hersbach et al. (2018).

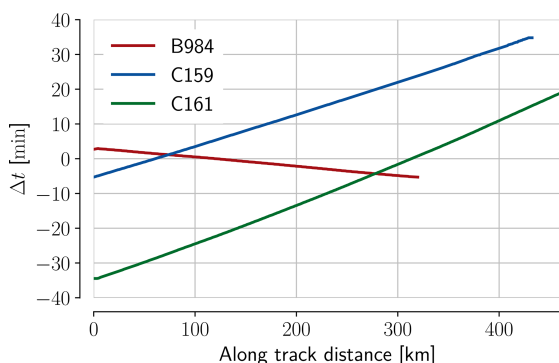


Figure 3. Delays between the co-located observations from radar and radiometers for the three flights.

model to the active and passive observations. Since the algorithm is described in detail in Pfreundschuh et al. (2020) the following section only outlines its main features and how it has been adapted to the flight data.

The retrieval input consists of a single radar profile and the corresponding spatially closest radiometer observations. Background properties of the atmosphere and the surface, such as temperature and wind speed, as well as a priori profiles for relative humidity and liquid cloud water are taken from the ERA5 hourly reanalysis (Hersbach et al., 2018).

The output of the retrieval are two parameters of the PSDs of frozen and liquid hydrometeors as well as liquid cloud water content (LCWC) and relative humidity. Hydrometeor PSDs are represented using the approach proposed by Delanoë et al. (2005): At each level in the atmosphere the concentration of hydrometeors with respect to the volume equivalent diameter D_{eq} is given by

$$N(D_{\text{eq}}) = N_0^* F\left(\frac{D_{\text{eq}}}{D_m}\right), \quad (1)$$

where F is a fixed function that specifies the shape of the normalized PSD, and N_0^* and D_m are the retrieved parameters. The N_0^* parameter is retrieved in log space while D_m is retrieved in linear space. Relative humidity is retrieved in a transformed space based on an inverse hyperbolic tangent transformation and cloud liquid water content in log space. A listing of all retrieval targets and corresponding a priori assumptions is provided in Table 2.

The forward model and retrieval were made adaptive so that the ingested observations can be easily adapted to the different sensors and channels that were available for each flight. Low-frequency channels that are used only over ocean surfaces are deactivated over land by setting the corresponding channel uncertainty to 10^6 K. The atmospheric grid was limited to altitudes between 0 and 10 km and matched to the resolution of the radar observations. The latest stable release

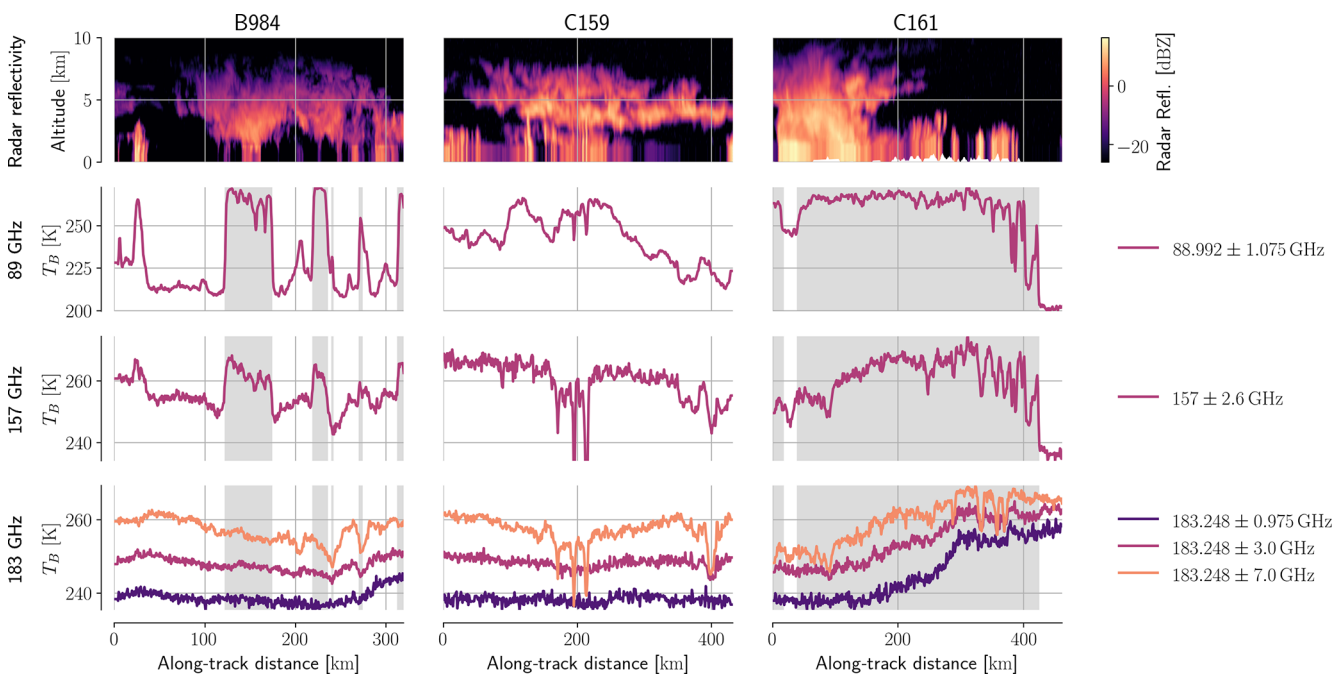


Figure 4. Passive microwave measurements from the MARSS radiometer together with the matched radar observations. Grey background in the radiance plots marks observations that were taken over land.

Table 2. Retrieval quantities and a priori assumptions used in the retrieval. The relation for the a priori mean of $\log_{10}(N_0^*)$ is taken from Cazenave et al. (2019).

Quantity	Retrieved parameters	A priori mean	A priori SD
Ice water content (IWC)	$\log_{10}(N_0^*)$	$-0.076586 \cdot (T - 273.15) + 17.948$ with T temperature in K	2
	D_m	Chosen so that $IWC = 10^{-6} \text{ kg m}^{-3}$ at all levels.	$500 \mu\text{m}$
Rain water content (RWC)	$\log_{10}(N_0^*)$	7	2
	D_m	$500 \mu\text{m}$	$500 \mu\text{m}$
Cloud liquid water content (CLWC)	$\log_{10}(\text{CLWC})$	From ERA5	1
Relative humidity (RH)	$\text{arctanh}(\frac{2 \cdot \text{RH}}{1.1} - 1.0)$	From ERA5	1

(version 2.4) of ARTS (Buehler et al., 2018) is used to implement the forward model used in the retrieval. The built-in single-scattering radar solver of ARTS is used to calculate radar observations and Jacobians. To account for the effect of multiple scattering in CloudSat observations, the attenuation due to hydrometeors is scaled at each atmospheric layer by a factor of 0.5 following Fig. 16 in Battaglia et al. (2010). Passive radiances are calculated using the ARTS interface to DISORT (Stamnes et al., 2000), and their Jacobians are approximated using a first-order scattering approximation. Gaseous absorption is modeled using the absorption models from Rosenkranz (1993) for N_2 and O_2 . Following Fox (2020), absorption from water vapor is calculated using

a combination of the AER database v3.6 (Cady-Pereira et al., 2020) for resonant absorption and the MT-CKD model version 3.2 for continuum absorption (Mlawer et al., 2012).

2.3.1 Representation of frozen hydrometeors

The forward model simulates active and passive observations in two steps: in the first one, the bulk properties that are used to represent hydrometeors in the retrieval are mapped to corresponding optical properties. The optical properties are then, in the second step, used together with background atmosphere and surface to simulate the observations.

The mapping of bulk to optical properties is based on a PSD and an ice particle habit that associates particles of dif-

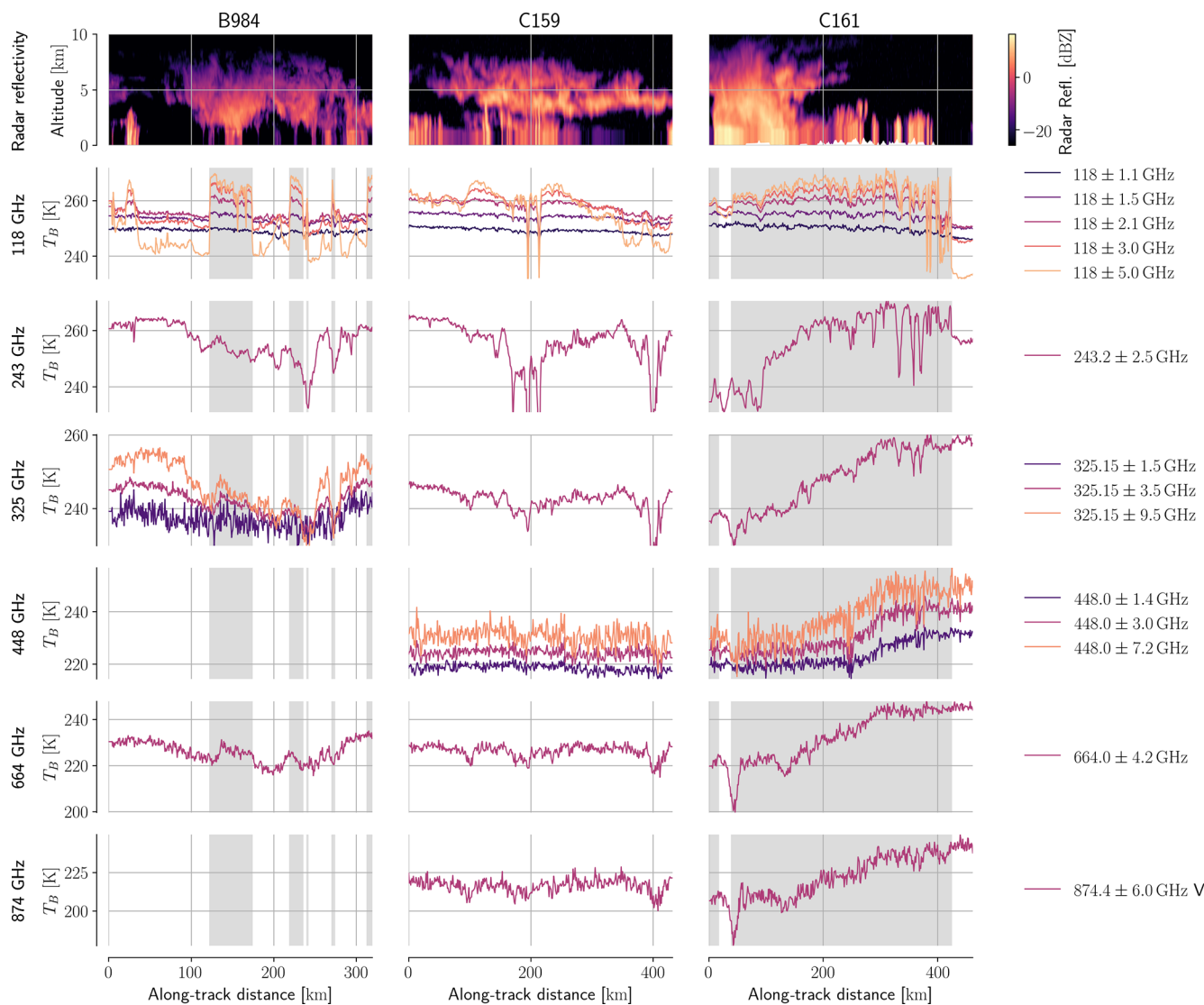


Figure 5. Passive microwave measurements from the ISMAR radiometer together with the matched radar observations. Grey background in the radiance plots marks observations that were taken over land and are therefore not used in the retrieval.

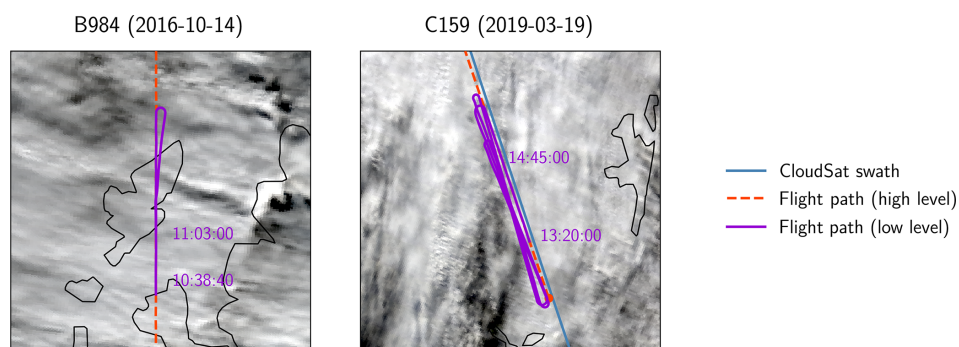


Figure 6. Detailed view of the flight paths of the high-level runs and in situ sampling paths for flights B984 and C159. The background is the true-color composite derived from the closest overpasses of the MODIS (MCST, 2017) sensor on the Aqua satellite.

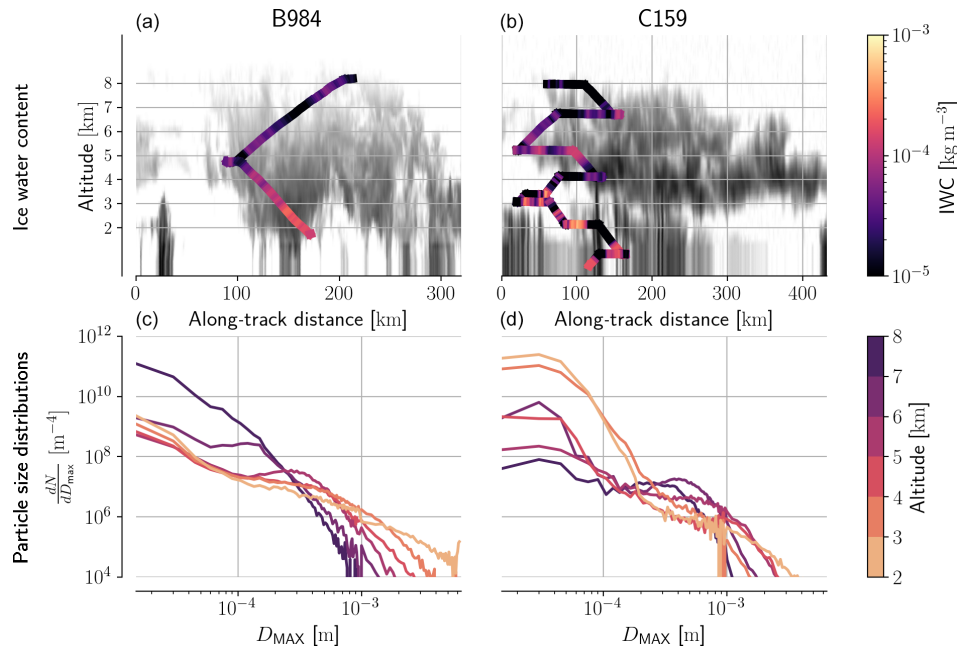


Figure 7. In situ-measured IWC and PSDs for flights B984 and C159. The first row of panels displays the measured IWC along the flight path plotted on top of the co-located radar observations. The second row displays the variation of the mean of the in situ-measured PSDs for different altitudes in the cloud.

ferent sizes and shapes to optical properties. As described above, the forward model uses the normalized PSD approach proposed by Delanoë et al. (2005) with the mass-weighted mean diameter (D_m) and intercept parameter (N_0^*) as parameters. The normalized shape function F in Eq. (1) follows a modified gamma distribution shape using the parameters from Cazenave et al. (2019). The ice particle habit is represented by a collection of ice particle shapes and corresponding, pre-computed single particle optical properties. Bulk optical properties are calculated by integrating the product of particle density and optical properties over the particle size. As the retrieval is currently set up, the particle habit cannot be retrieved and must be assumed a priori. Due to the large variability of ice particle shapes in real clouds, it is unclear which particle habit should be chosen to best represent their radiative properties or whether such a unique best model exists at all. Hence, the approach taken here is to select a set of habits and perform the retrieval with each of them. This will allow us to investigate the impact of the selected habit on the retrieval results.

Five particles were selected from the set of standard habits that is distributed with the ARTS SSDB (Eriksson et al., 2018). The standard habits are particle mixes that combine pristine crystals at small sizes with aggregate shapes at larger sizes. The selected habits are listed in Table 3. To provide an overview of their optical properties, characteristic bulk optical properties have been calculated and displayed in Fig. 8 together with their mass–size relationships. The PSD used to calculate the bulk optical properties is the same that is used

in the retrieval with the N_0^* value set to the a priori value at a temperature of 260 K. The particles were selected so that their properties cover most of the variability of the available set of standard habits both in terms of the mass–size relation as well as their optical properties.

Complementary information that can help guide the selection of a suitable particle shape can be obtained from in situ measurements. Since the particle habit associates particle sizes with a specific shape it can be used to compute a bulk water content corresponding to PSD measurements. This allows calculating the IWC corresponding to the in situ-measured PSDs, which can be compared with the IWC measured by the Nevzorov probe. The agreement between the PSD-derived IWC and the in situ-measured IWC can then provide insight into whether the mass–size relation corresponding to the particle shape is consistent with that of the particles in the cloud. Such a comparison is provided in Fig. 9.

For both flights, the large plate aggregate and the six-bullet rosette yield the best overall agreement with the in situ-measured IWC. The large column aggregate yields values at the low end of the measured distribution for all flights and altitudes. The Evans Snow Aggregate yields similar results to those of the large column aggregate except at high altitudes for flight B984 and low altitudes for flight C159. The eight-column aggregate generally yields higher IWC values than most other habits and tends to overestimate the in situ IWC at low altitudes for flight B984.

Table 3. Particle habits used in the retrieval. The mass–size relationship is given in terms of the parameters of a fitted power law of the form $m = \alpha \cdot D_{\text{MAX}}^\beta$ with D_{MAX} the maximum diameter and m in kg.

Habit name	Shapes used Name (ID)	Size range		Mass–size relationship	
		$D_{\text{eq, min}}$ (μm)	$D_{\text{eq, max}}$ (μm)	α	β
Six-bullet rosette	Six-bullet rosette (6)	16	8905	0.4927	2.4278
Eight-column aggregate	Eight-column aggregate (8)	10	3000	440	3
Evans snow aggregate	Evans snow aggregate (1)	50	2109	0.196	2.386
Large plate aggregate	Thick plate (15)	16	200	110	3
	Large plate aggregate (20)	160	3021	0.21	2.26
Large column aggregate	Block column (12)	10	200	110	3
	Large column aggregate (18)	160	3021	0.25	2.43

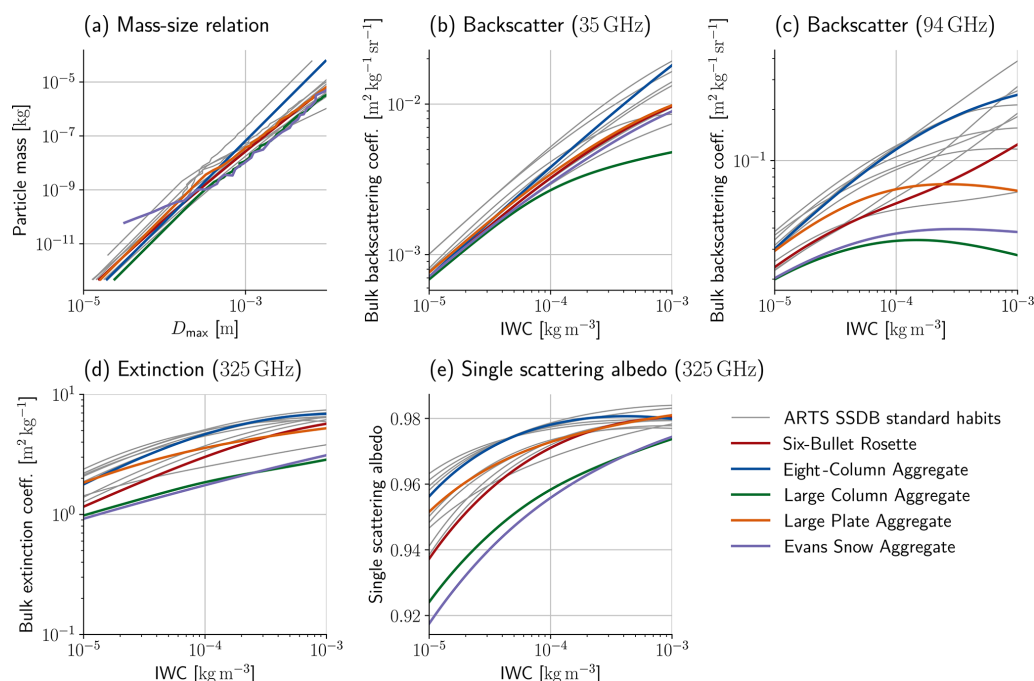


Figure 8. Properties of the selected ice particle shapes that are used to represent frozen hydrometeors in the retrieval forward model. Colored lines display the properties of the selected habits, while grey lines show the properties of the remaining standard habits distributed with the ARTS SSDB. Bulk optical properties were calculated using the PSD parametrization that is used in the retrieval.

3 Results

The primary results of the combined retrieval are the retrieved hydrometeor size distributions. In addition to that, the retrieval also fits a radiative transfer model to the observations whose agreement with the real observations can provide valuable information regarding the accuracy of the forward model and the fitness of a priori and modeling assumptions.

3.1 Fit to observations

The retrieval residuals, i.e., the difference between simulated and real observations, for the large plate aggregate habit are displayed in Fig. 10. As the figure shows, the retrieval was able to fit both radar and radiometer observations fairly well for all flights. For flight B984, the radar residuals show some scattered deviations located at the edge of the cloud, which are likely discretization artifacts. Except for that, residuals for this flight remain well within 1 dB. The residuals for flight C159 exhibit four vertical stripes with significant residuals in the radar observations. In these regions, which correspond to

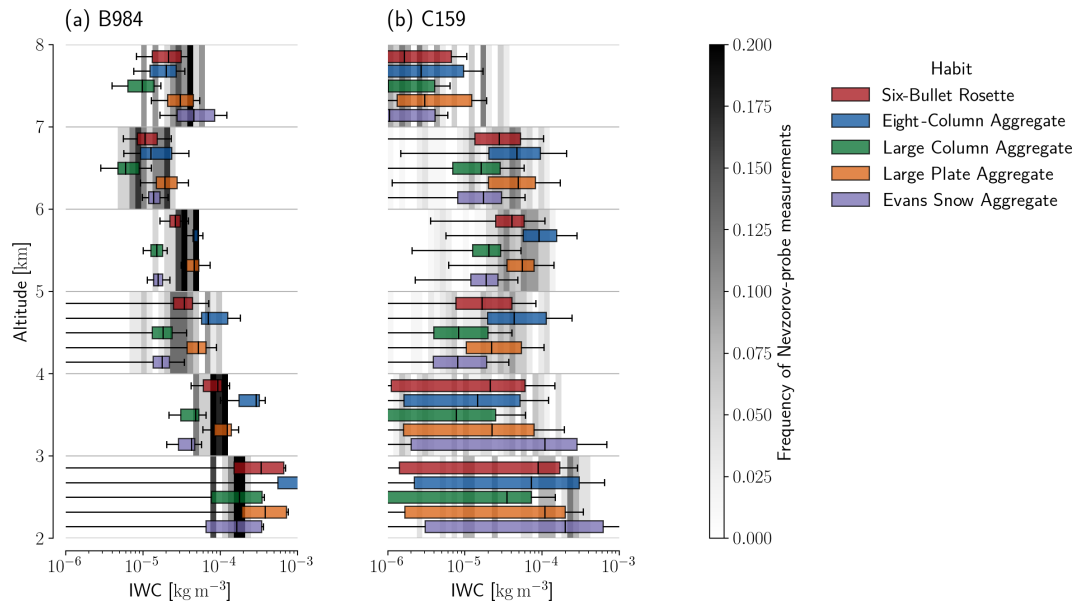


Figure 9. Comparison of bulk IWC as measured by the Nevzorov probe and inferred from in situ-measured PSDs using a given particle shape. The background in each plot shows the distribution of Nevzorov-measured IWC for a given 1 km altitude bin. Colored boxes display the distribution of IWC in that bin inferred for a given particle shape. Boxes, whiskers and outliers are drawn following Tukey's conventions for box plots.

significant scattering depressions in most passive channels up to 325 GHz, the simulations overestimate the radar reflectivity. Apart from this, there are some smaller regions where the simulations underestimate the radar reflectivity, but these remain limited to within few dB. For flight C161, moderate negative residuals in the radar observations can be observed in the right half of the convective core, which coincide with an overestimation of the scattering signal at 243 GHz.

Radiometer residuals for flight B984 are mostly within ± 5 K but larger for flights C159 and C161. For these two flights, residuals exceeding 10 K are observed in the window channels up to 243 GHz as well as the outermost channels around the absorption lines at 118 and 183 GHz. Since these occur in profiles where precipitation is present and in which similar residuals can be observed in the radar observations and other channels that are sensitive to the lower parts of the atmosphere, a likely explanation is that they are caused by precipitation that is not observed by all sensors due to spatial and temporal co-location issues. In particular, the large residuals in the 243 GHz channel for flight C161 at around 100 km along-track distance may well be caused by the evolution of the convective cloud during the delay of about 30 min that separates the radiometer and radar observations.

For a more systematic analysis of the effect of the assumed particle shape on the retrieval residuals, their distribution for radar and radiometer channels around 183 GHz and above are displayed in Fig. 11. The distributions, which for most channels are close to or centered around zero, confirm that the retrieval generally fits the observations well. The

largest deviations are observed for the 874 GHz channel and the 243 GHz channel for flight C161. For flights C159 and C161, the 874 and 664 GHz channels exhibit small systematic biases of opposite signs, which may indicate issues with the calibration or the modeling of water vapor absorption at these channels. Furthermore, it is interesting to note that the ice particle habit only has a minor impact on the residuals, indicating that the retrieval can compensate for mismatches in the assumed particle shape by adjusting the retrieval variables.

3.2 Retrieved ice water content

The retrieved bulk IWC and corresponding IWP for all three cloud scenes are displayed in Fig. 12. For all three flights, the ice particle shape has a significant effect on the retrieved amount of ice. In terms of IWP, the large-column aggregate and Evans snow aggregate habits yield the highest values, while the eight-column aggregate consistently yields the lowest IWP. The large plate aggregate and six-bullet rosette both yield values within the range of the other particle models with the six-bullet rosette leading to slightly higher IWP values than the large plate aggregate. In addition to the effect of the increased total retrieved water content, the particle habit also has a small effect on the vertical distribution of the ice hydrometeors, which is visible particularly for retrieved IWC in the convective core observed during flight C161.

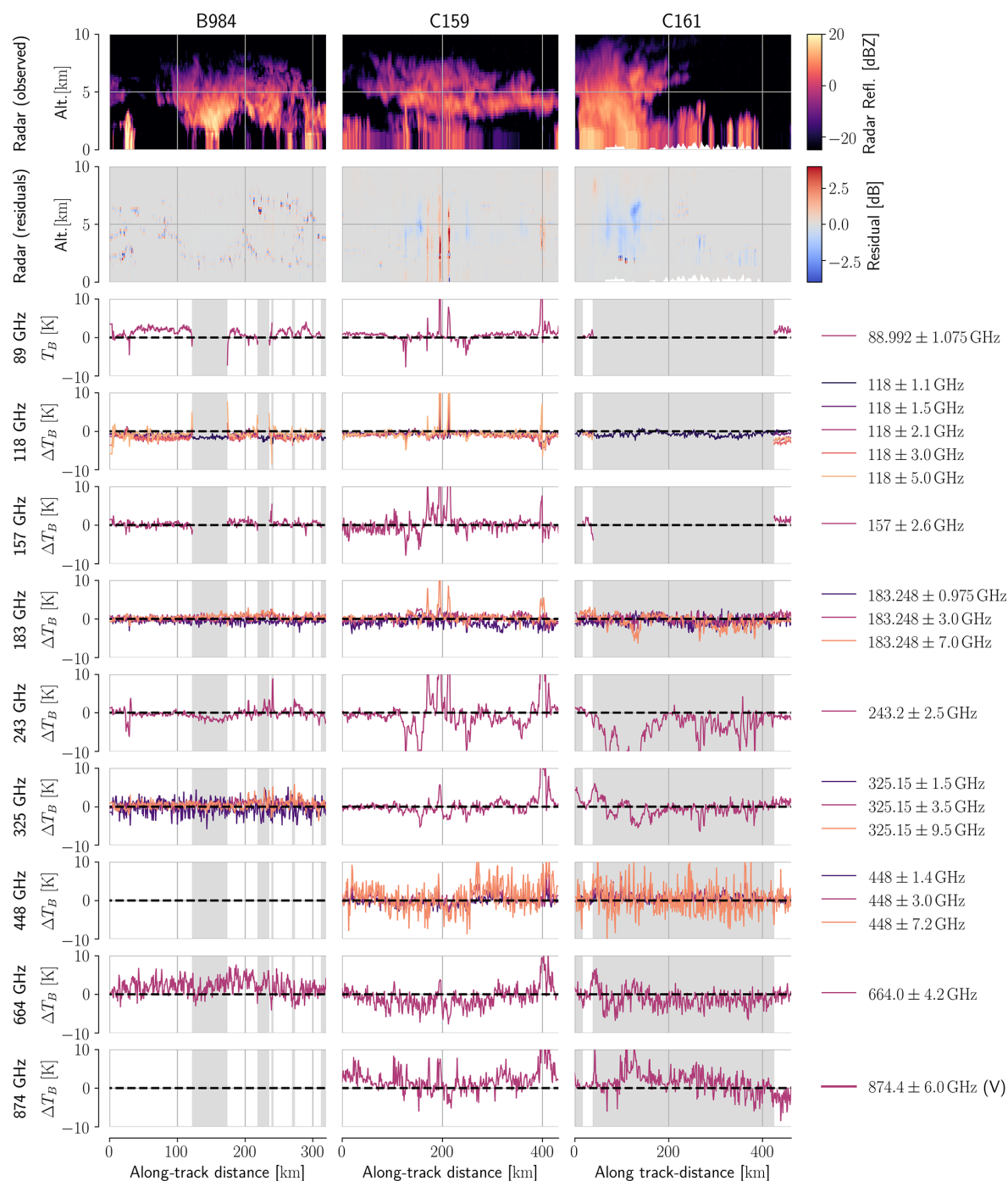


Figure 10. Differences between observed and fitted observations for the large plate aggregate particle. The first two rows depict the radar observations and their residuals, respectively. The following rows show the retrieval residual in the radiometer measurements for each of the frequency bands used in the retrieval. The grey shading marks sections of the flight path that were located over land surfaces.

3.3 Comparison to in situ measurements

The most important question regarding the hydrometeor retrieval is certainly whether the retrieved bulk properties are consistent with the in situ measurements. To compare the in situ measurements to the retrieval results, they were mapped

to the radar observations using a nearest-neighbor criterion. For B984, retrieval results within a distance of 1 km of the flight path were then associated with the in situ measurements. Because of the mismatch between observations and in situ sampling paths, another approach was taken for flight C159. Here the retrieval results were mapped to the in situ

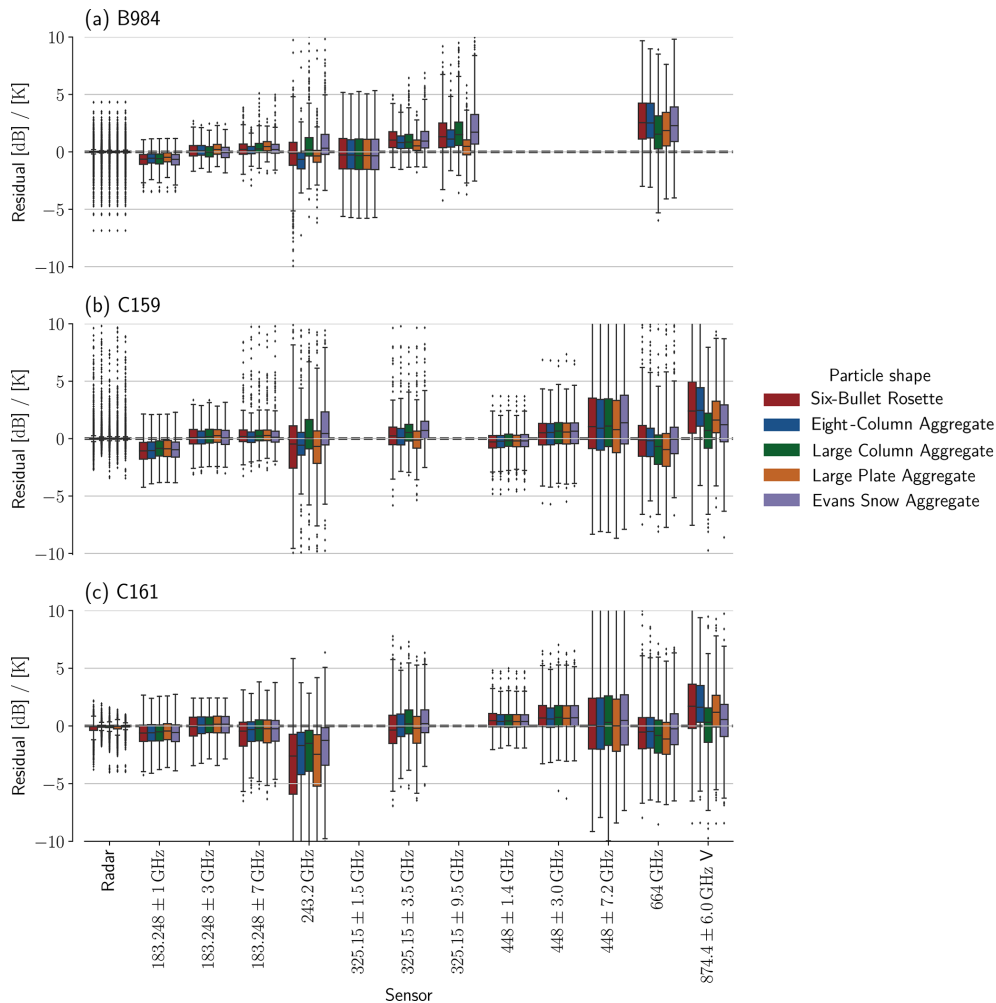


Figure 11. Distributions of retrieval residuals for different particle shapes used in the forward model for each of the three flights.

measurements by selecting all retrieval results between 50 and 150 km along-track distance. Both the matched retrieval results and the vertically resolved distributions of measured and retrieved IWC are displayed in Fig. 13.

For flight B984, the distribution of in situ-measured IWC values is well within the range of retrieved IWC values across all particle shapes up to an altitude of around 7 km. At these altitudes, the best match to the in situ measurements is achieved with the six-bullet rosette particle and the large plate aggregate. The eight-column aggregate underestimates the in situ-measured IWC while the large column aggregate and Evans snow aggregate overestimate it. Above 7 km all particles lead to results that underestimate the in situ-measured IWC. A likely cause for this is the high concentration of small particles as observed in the in situ measurements (see Fig. 7) for which microwave observations lack sensitivity.

For flight C159, the distribution of retrieved IWC still covers the distribution of in situ-measured values for altitudes above 3 km but exhibits a tendency towards underestima-

tion. Overall, the differences between the results for different habits are smaller for this flight. However, the uncertainties caused by the large sampling region as well as the potential co-location issues affecting the results make them less conclusive.

Finally, we want to address the question whether the representation of cloud microphysics within the retrieval forward model is consistent with the in situ-measured PSDs. For this, we calculate the PSDs corresponding to the retrieved bulk properties and compare them to the in situ measurements. The results of the comparison are displayed in Fig. 14. For flight B984, we find good agreement between retrieved and in situ-measured PSDs for larger particles ($D_{\text{MAX}} > 200 \mu\text{m}$) for the large plate aggregate and the six-bullet rosette. Since this is observed even at altitudes above 6 km, it confirms that the underestimation of IWC at these altitudes is likely caused by the high concentration of smaller ice particles. For flight C159, the retrieved PSDs deviate significantly from the in situ measurements. Although the six-bullet rosette and large plate aggregate seem to fit the tail ($D_{\text{MAX}} > 1 \text{ mm}$) of the

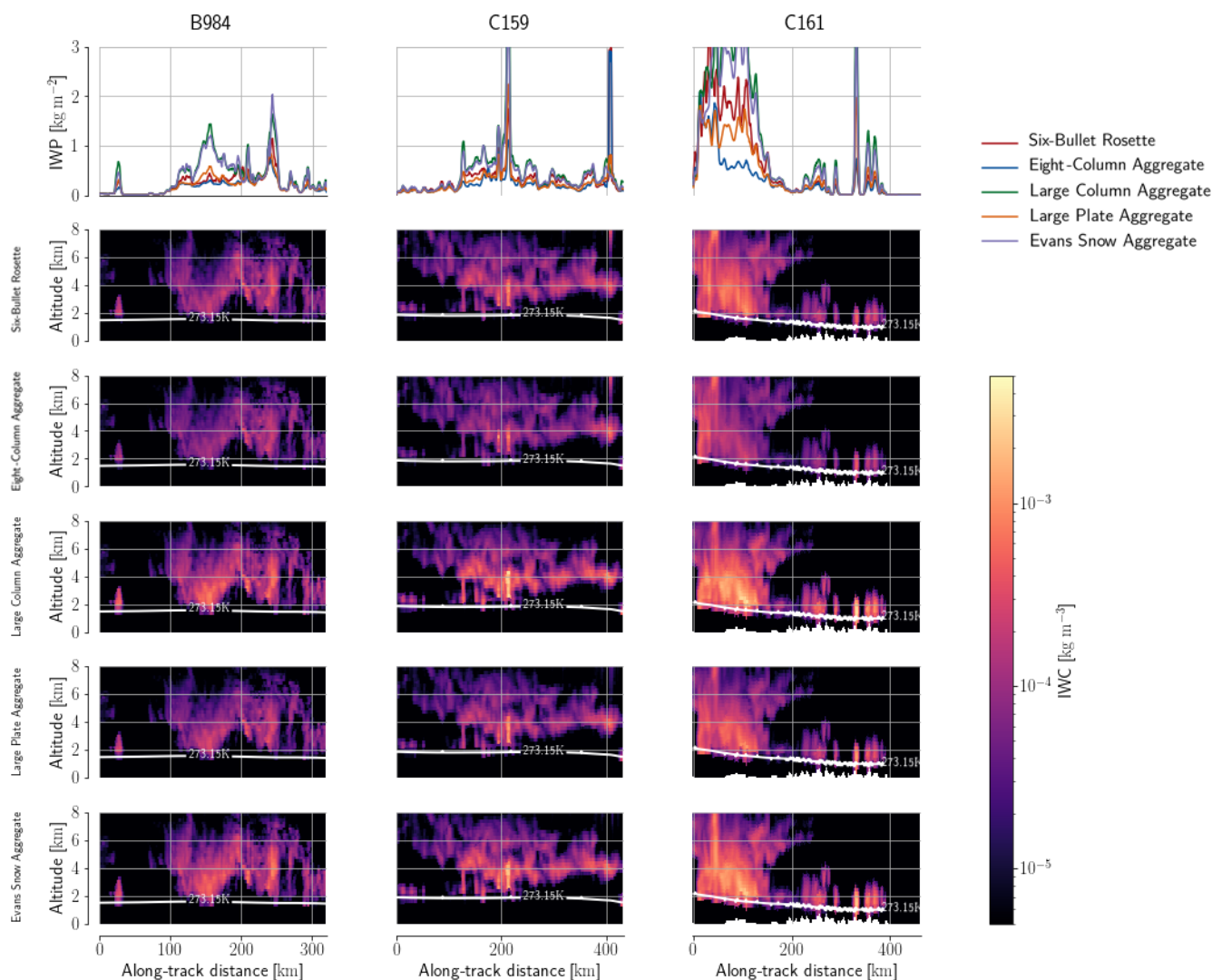


Figure 12. Retrieved IWP and IWC content for all flights and different ice particle shapes assumed in the retrieval. The white line displays the ERA5 freezing level from Hersbach et al. (2018).

PSD for most altitudes except between 3–4 km, the measured PSDs deviate considerably at smaller sizes. This may also indicate that the assumed shape of the PSD may not be suitable for the observed cloud system.

4 Discussion

This study used a novel, synergistic retrieval to retrieve vertically resolved distributions of ice hydrometeors from co-located radar and microwave radiometer observations. For most of the considered channels, the retrieval succeeded in fitting both the active and passive observations without significant, systematic deviations. For two of the flights, the retrieved hydrometeor distributions were compared to in situ measurements. For one of the flights (B984), we found good agreement with the in situ-measured bulk IWC for altitudes

between 2 and 6 km for two of the particle shapes. The same particle shapes also yield the best agreements with the in situ-measured PSDs for larger ice particles ($D_{\text{MAX}} > 200 \mu\text{m}$). For the second flight (C159), no consistency was found between the in situ measurements and the retrieval. A likely explanation for this is that the in situ measurements are not as well co-located due to the temporal and spatial differences between the different observations as well as the in situ measurements.

4.1 Sub-millimeter radiative transfer in cloudy atmospheres

A first important result of this study is the ability of the retrieval to find atmospheric states that are consistent with the observed radiances and radar reflectivities for all three flights. This in itself is not self-evident due to the uncertain-

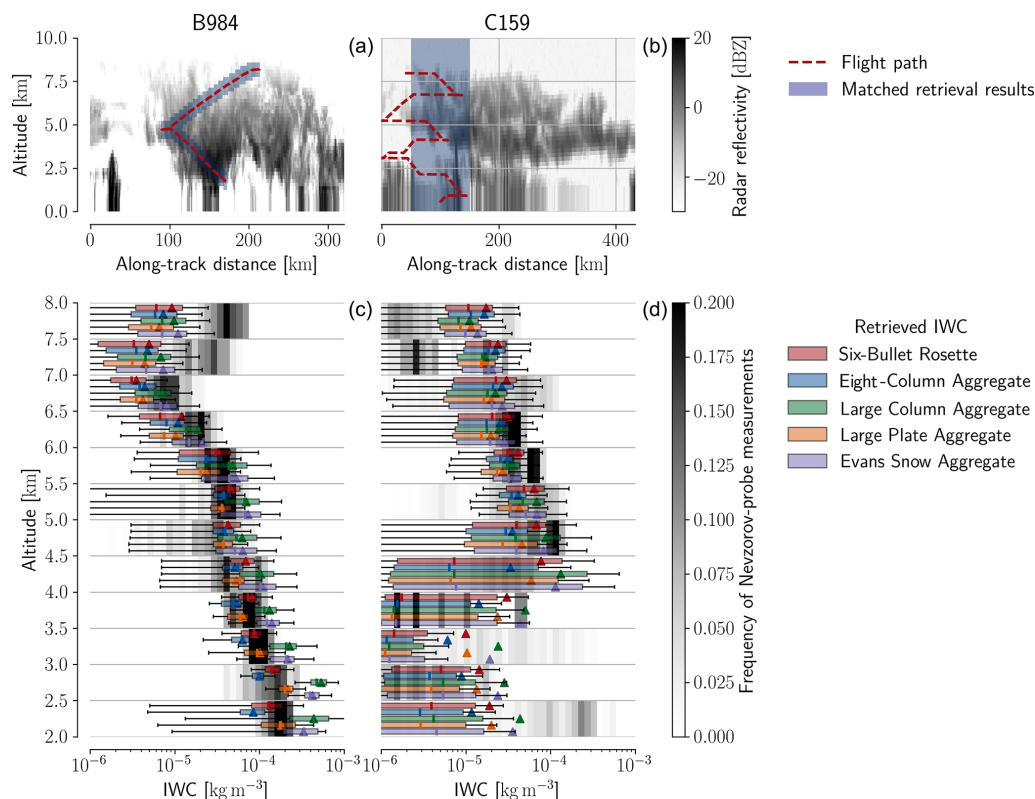


Figure 13. In situ-measured and retrieved IWC for flights B984 and C159. Panels (a) and (b) show the in situ sampling paths in relation to the measured radar reflectivity as well as the retrieval values that are mapped to the in situ measurements (blue shading). Panels (c) and (d) show in the background the distribution of in situ-measured IWC values in altitude bins with a height of 500 m. Colored boxes display the corresponding distribution of retrieved IWC values for different ice particle shapes. Boxes are drawn following Tukey's conventions for box plots. The colored triangles mark the mean of the distribution.

ties that still affect the modeling of ice-particle scattering at millimeter and sub-millimeter wavelengths. Previous studies that tried to directly validate sub-millimeter RT through clouds were limited to either tropical clouds (Evans et al., 2005; Eriksson et al., 2007) or cirrus clouds (Fox et al., 2017). For flight B984, the radar and all passive observations were fitted up to small systematic biases no larger than 3 K. The deviations for the two other flights were generally larger, but these were likely caused by spatial and temporal co-location errors. This indicates that both the assumed optical properties as well as the retrieval forward model are consistent across the considered wavelengths. Furthermore, the two particle shapes for which the best agreement between retrieved and in situ-measured hydrometeor distributions was found for flight B984 were also those whose mass–size relationship yielded the best agreement between in situ measurements of IWC and PSDs. Since this ties the microphysical properties of the particles to their optical properties, it suggests that the modeling of these particles in the ARTS SSDB is physically consistent.

4.2 The impact of assumed ice particle shape

A rather unexpected result that emerged from this study is that the retrieval can fit the observations fairly well regardless of the assumed ice particle shape. This indicates that although the observations are sensitive to variations in ice particle shape, they alone cannot constrain it. This is in agreement with what has been reported in Pfreundschuh et al. (2020), namely that no correlation could be found between the particle shape yielding the best retrieval fit and the one yielding the most accurate retrieval results.

In an effort to better separate a potential signal from the ice particle shape in the retrieval residuals, we have investigated the relationship between retrieved IWP and the residual for different channels. Most channels that were available on all flights do not show a clear sign of a relation between the particle shape and the residuals. As an example for those channels we provide scatter plots of the retrieved IWP and the channel residual for the 325 ± 3.5 GHz channel in Fig. A1 in the Appendix. We did, however, identify two channels from flight B984 that may exhibit a potential signal from the ice particle shape in the residuals. The scatter plots for these two channels are provided in Fig. 15. For the 325 ± 9.5 GHz

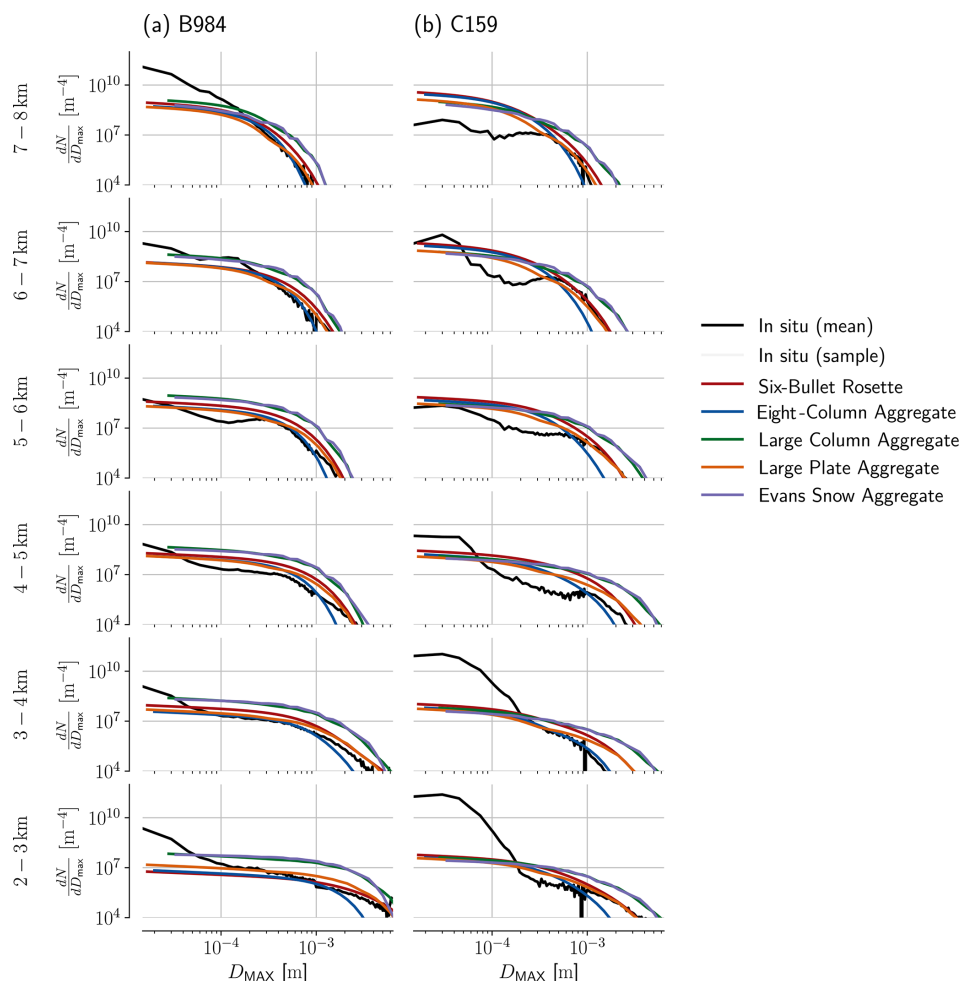


Figure 14. In situ-measured and retrieved PSDs for flights B984 (left column) and C159 (right column). Each row of panels shows the mean of the in situ-measured PSDs (black) together with randomly drawn samples of measured PSDs (light grey) for a given altitude bin of a height of 1 km. Colored lines on top show the corresponding mean retrieved PSD for different assumed particle shapes.

channel, all tested particles except the large plate aggregate seem to manifest a positive correlation between IWP and the residuals. For the 243 ± 2.5 GHz, the six-bullet rosette, eight-column aggregate and large plate aggregate exhibit a weak negative trend in the residuals, while it remains positive for the large column aggregate and Evans snow aggregate. At least for these two channels the large plate aggregate seems to stand out as the ice particle shape yielding the smallest residuals across the retrieved range of IWP values.

Since the large plate aggregate is one of the particles for which the best agreement between retrieved and in situ measurements was obtained, this may be viewed as an encouraging result indicating that sub-millimeter observations can, at least in combination with radar observations, be used to constrain the shape of ice particles in clouds. However, taking into account that these are observations from only one flight as well as the complicated statistics of the results from Fig. 15, it remains unclear whether these findings are statistically significant. A potential confounding factor may be

the impact of the a priori assumptions on these results. Since the retrieval balances the residual with the deviation from the a priori, this may lead to a worse fit for the softer particles (large column aggregate, Evans snow flake) for which a much higher D_m must be retrieved for a similar scattering effect. While this effect may be desired in the retrieval to avoid the apparently excessive amounts of ice retrieved using these particle shapes, it is the combination of observations and a priori assumptions that constrains the particle shape and not the observations alone. We present these results here mainly for completeness and to serve as a potential basis for further investigation.

Nonetheless, even if indeed present, a potential signal from the ice particle shape in the results would be limited to a few Kelvin. This implies that future ice hydrometeor retrievals that make use of millimeter and sub-millimeter microwave observations must either account for the uncertainty caused by variations in ice particle shape or find ways to more accurately constrain the shape a priori. Moreover, for

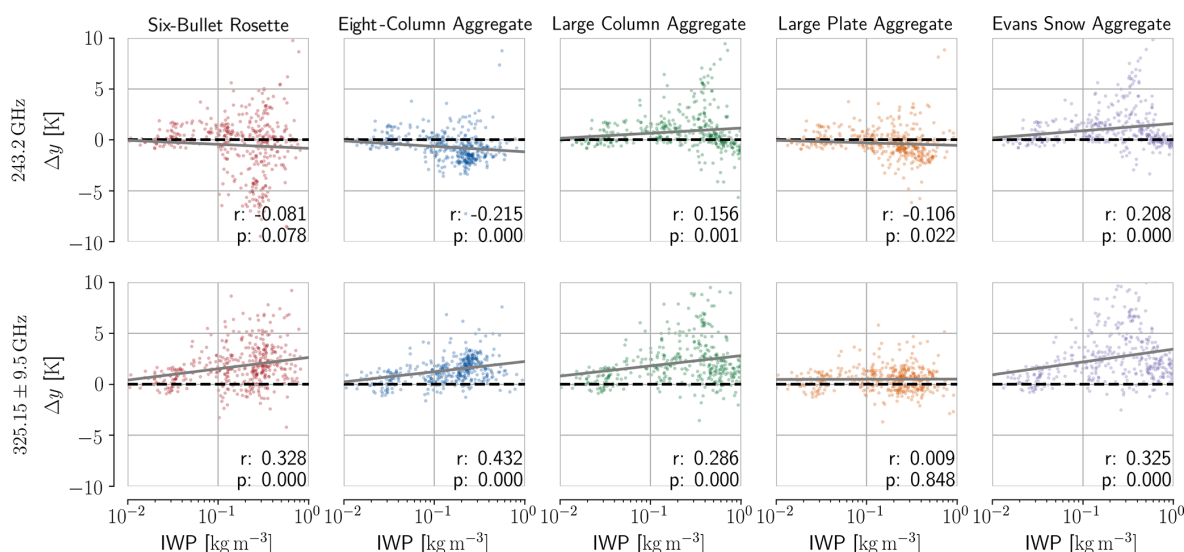


Figure 15. Brightness temperature residuals between true and simulated observations for two channels from flight B984. The first row shows the results for the 243 ± 2.5 GHz channel, while the second row shows the results for the 325 ± 9.5 GHz channel. Columns show the results for the five tested particle shapes. The grey line in each panel represents the regression line for the plotted data points. The text displays the correlation coefficient r and the p value of a two-sided significance test for the slope of regression line.

studies that seek to validate model predictions by comparing simulated and observed microwave observations, this implies that care must be taken to accurately characterize the ice particle shape. This is because agreement up to a few Kelvin between simulations and observations can be achieved for bulk water contents that vary by almost an order of magnitude (see Fig. 12).

4.3 Representation of cloud microphysics

The lack of a distinct signal that constrains the ice particle shape even in the combined observations puts additional weight on the question of how to best represent ice particles in simulations of microwave observations. The habits that lead to the most accurate retrieval results in this study were the large plate aggregate and the six-bullet rosette. The channel residuals presented in Fig. 15 indicate the best fit for the large plate aggregate although it is unclear how robust these findings are. Furthermore, it is interesting to note that the large plate aggregate was also found to yield the best agreement between simulations based on a numerical weather prediction (NWP) model and satellite observations at frequencies between 19 and 190 GHz for stratiform snow in Geer (2021).

Nonetheless, these findings are based on observations from the single flight for which the retrieval results could be reliably compared with in situ measurements. This result can thus be seen as indication that these habits may work well for similar mid-latitude cloud systems, but more generally applicable conclusions would require further and more systematic investigation.

4.4 Retrieval validation

Since the results presented in Pfreundschuh et al. (2020) were limited to simulations based on a high-resolution climate model, the validation of the retrieval using real observations remained an open issue. For flight B984, good agreement was found between retrieval results and in situ measurements. Although the retrieved IWC deviates from the in situ measurements at altitudes > 6 km, the retrieved PSDs still match the in situ measurements well for particles with $D_{\text{MAX}} > 200 \mu\text{m}$. This indicates that the concentrations of these larger particles may be retrieved correctly but that the total IWC is underestimated due to the mismatch between assumed and actual PSD shape, the former of which lacks the very high concentration of small particles that are present in the in situ measurements. Although O'Shea et al. (2021) and O'Shea et al. (2019) show that the occurrence of high particle concentrations at sizes below $200 \mu\text{m}$ may be due to measurement inaccuracies of the CIP-15 probe, the measured PSDs correctly reproduce the measured IWC at these altitudes when the corresponding water content is calculated using any of the tested particle habits (Fig. 9). Furthermore, the presence of a cloud layer with a large number of small particles was also reported by Ewald et al. (2021) who investigated the same cloud system with combined radar–lidar observations.

For flight C159 no good agreement was found between retrieved and in situ-measured IWC and PSDs. However, some evidence suggest that this may be due to co-location: firstly, the flight path for the in situ sampling was found to be offset from the high-level run during which the observations were

taken in the direction opposite to the wind at 800 mb (Figs. 1, 6). Secondly, a clear backscattering signal is present in the CloudSat CPR observations even in regions where only negligible amounts of IWC are present in the in situ measurements (Fig. 13). Thirdly, the residuals observed in Fig. 10 are indicative of additional co-location issues between radar and radiometer observations. Finally, also the comparison of retrieved and in situ-measured PSDs (Fig. 14) seems to indicate large deviations between the observed and the assumed PSD shape.

4.5 The added value synergistic cloud retrievals

Although the evidence from flight B984 suggests that the synergistic retrieval algorithm works well for retrieving ice hydrometeor concentrations, similar retrievals can be performed using only radar observations. A retrieval using only radar observations has the obvious advantage of requiring only a single sensor and being computationally much less complex. This naturally leads to the question of the added value that a synergistic retrieval can provide.

To investigate this, the results of the combined and an equivalent radar-only retrieval for flight B984 are displayed in Fig. 16. For the large plate aggregate and six-bullet-rosette habits, the results of the combined and the radar-only retrieval are largely similar down to an altitude of about 3.5 km, below which the radar-only retrieval tends to overestimate the in situ IWC. In contrast to the combined retrieval, the results of the radar-only retrieval exhibit almost no impact from the particle habit. While the radar-only retrieval remains mostly unaffected by the habit choice, using a different habit in the combined retrieval may cause systematic overestimation (Evans snow aggregate and large column aggregate) or underestimation (eight-COLUMN AGGREGate).

A similar comparison is shown in Fig. 17 for the retrieved PSDs. The PSDs are largely similar for both retrievals for altitudes above 4 km. Below that, however, the radar-only retrieval overestimates the particle concentrations, while the combined retrieval matches the in situ measurements well for the large plate aggregate and six-bullet rosette habits. This indicates that the combined retrieval utilizes the complementary information in the radar and passive observations to match both moments of the PSD, whereas the radar-only retrieval can only match one of them.

The tendencies observed for the retrieved IWC in Fig. 14 are even more pronounced when the IWP is calculated along the sampling path of the in situ measurements. The resulting retrieved IWP values are displayed in Table 4. The radar-only retrieval systematically overestimates the reference IWP for all tested particle shapes. The combined retrieval leads to even stronger overestimation when the large column aggregate or the Evans snow aggregate are used as ice particle shapes, while the eight-column aggregate leads to a strong underestimation of the true IWP. With the six-bullet rosette and the large plate aggregate used as ice particle shapes, the

Table 4. Retrieved IWP along in situ flight path for flight B984 for the combined and radar-only retrieval.

IWP (kg m^{-2})		
In situ	0.3615	
Habit	Combined	Radar-only
Six-bullet rosette	0.3362	0.4971
Eight-column aggregate	0.2383	0.6783
Large column aggregate	0.7868	0.4116
Large plate aggregate	0.3666	0.4664
Evans snow aggregate	0.7082	0.5073

combined retrieval yields results that are closest to the in situ measurements. Thus, while the incorporation of passive observations increases the sensitivity to the representation of hydrometeors, it can help to improve the retrieval of IWP given that a suitable particle model is used in the retrieval.

These results thus suggest that combining radar with passive microwave observations helps to constrain the PSD of ice hydrometeors for sufficiently large particle sizes ($D_{\text{MAX}} > 200 \mu\text{m}$). Since for air- and space-borne observations only microwave observations can sense the base of thick clouds, this is a unique synergy between these types of observations.

While these results were obtained for a Ka band cloud radar, we do not expect them to change much for a W band radar. Although the habit may have a stronger effect on the retrieval results of a W band radar due to its higher frequency, the underlying problem remains that the radar observations provide only a single piece of information per range bin. To retrieve the two moments of the hydrometeor PSD, the retrieval thus has to rely on a priori information, which cannot accurately describe the distributions in all clouds. Although the passive observations provide only a comparably small amount of additional information, our results indicate that the retrieval is able to use that to better constrain the retrieved hydrometeor distributions.

4.6 Limitations

Since microwave radiative transfer simulations in cloudy atmospheres remain a challenging problem, it is important to also consider the limitations of the simulations and derived results that were presented in this study. The simplifications that were applied in the simulations are the following:

1. Horizontal photon transport between the retrieved profiles is ignored.
2. Inhomogeneity across the radar and radiometer beams is ignored.
3. The finite spectral resolution of the passive channels is neglected.

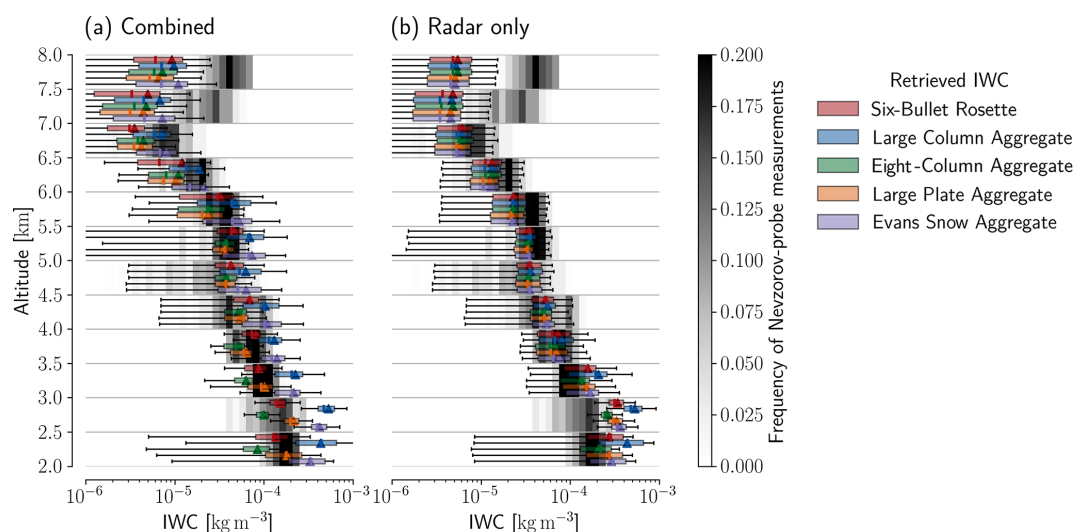


Figure 16. In situ-measured and retrieved PSDs for flight B984 for the combined and the radar-only retrieval. Each panel displays the distributions of in situ-measured IWC for different altitude bins in the background and the distribution of retrieved IWC values for different ice habits as colored boxes on top.

4. The radar solver neglects multiple scattering.
5. The effects of particle orientation are ignored.

Barlakas and Eriksson (2020) found that neglecting photon transport in simulations of sub-millimeter observations across a footprint of 6 km incurs only a small random error with biases < 0.5 K, so it is likely also small for the simulations presented here. For flight B984, the horizontal averaging of the radar observations leads to a profile width of 700 m which is fairly close to the width of the radiometer field of view which varies between about 900 and 200 m at an altitude of 5 km. The effect of beam inhomogeneity is therefore expected to be small for this flight. For flights C159 and C161, the radar beam has an along-track width of about 1.4 km, which is larger than that of the radiometers, so these observations may be affected to a larger extent than those for flight B984.

Neglecting the finite spectral resolution of the passive channels can lead to an error of up to 2.1 K for satellite observations that are affected by ozone absorption (Eriksson et al., 2020). Since the passive observations used in this study were all taken from altitudes below 10 km the effect of this approximation is likely negligible.

The effect of multiple scattering for air-borne radar observations is generally negligible (Battaglia et al., 2010). For CloudSat observations, however, the higher frequency and the considerably wider footprint will increase the effects of multiple scattering on the observations. Although the simulations account for the signal-enhancing effect of multiple scattering by layer-wise reduction of the attenuation, the presence of multiple scattering may still add to the uncertainty in the simulations for flights C159 and C161.

Finally, there is the potential presence of oriented particles in the cloud. The different ice habits used in this study all assume totally random orientation of the ice particles. Systematic vertical orientation of particles of a given shape in the cloud would effectively alter their scattering properties. For observations at nadir, particle orientation can increase the extinction of the large plate aggregate of up to 20 % (Barlakas et al., 2021). To first order, the increase in extinction can be expected to cause a similar overestimation of the retrieved IWC. This, however, is still considerably lower than the differences observed due to different ice habits.

5 Conclusions

The main result from the experiments presented in this study is that we were able to find two ice particle shapes, the large plate aggregate and the six-bullet rosette, for which the results of the combined retrieval were consistent with the observations as well as the in situ-measured IWC and PSDs for flight B984. Considering the co-location issues that likely affected the other two flights, we interpret this as a cautious indication of the validity of the retrieval implementation. Since the ARTS radiative transfer model and optical properties from the ARTS single-scattering database constitute a crucial component of the retrieval, this result also indicates that they work reliably across the millimeter- and sub-millimeter domain.

The results confirm the simulation-based findings from Pfreundschuh et al. (2020) that a synergistic retrieval based on active and passive microwave observations can help to characterize the PSD of large ice hydrometeors ($D_{\text{MAX}} > 200 \mu\text{m}$) better than a radar-only retrieval alone. This indi-

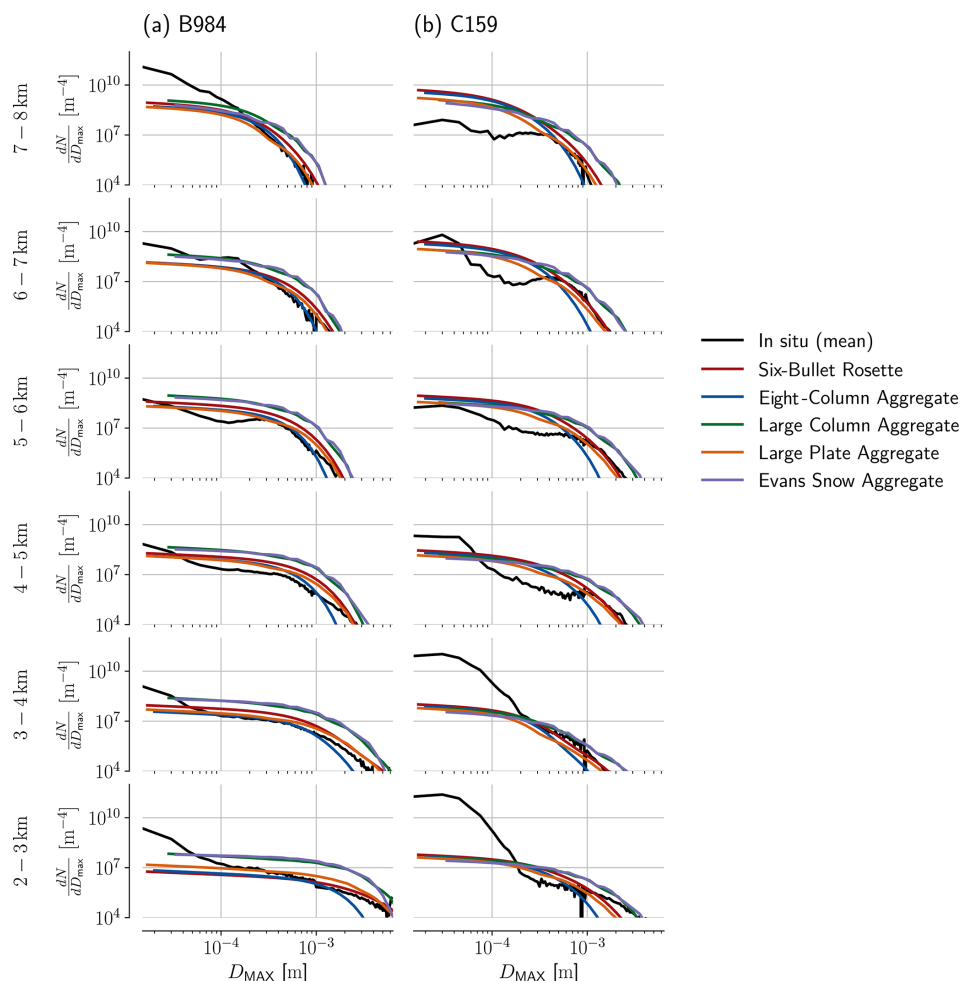


Figure 17. In situ-measured and retrieved PSDs for flight B984 retrieved using the combined (a) and the radar-only retrieval (b). Each row of panels shows the mean of the in situ-measured PSDs (black) together with randomly drawn samples of measured PSDs (light grey) for a given altitude bin of a height of 1 km. Colored lines on top show the corresponding mean retrieved PSD for different assumed particle shapes.

cates that such retrievals can be used to study the microphysical properties of clouds and thus help to improve their representation in weather and climate models.

However, the retrieval is at the same time very sensitive to the assumed ice particle habit that is used in the retrieval forward model. Although we found some evidence of a signal that could help to constrain the ice particle shape based on the combination of radar and sub-millimeter observations, it remains limited to not more than 5 K. This means that more work is needed to find out how to effectively constrain the ice particle shape with remote-sensing observations or to better constrain it a priori.

Although further work will be required, this study demonstrates the feasibility and potential of synergistic retrievals of ice hydrometeors by combining active and passive observations at millimeter and sub-millimeter wavelengths. Since the combined retrieval can better constrain the PSD of ice hydrometeors, it may be a useful tool to study the representation of clouds in NWP and climate models. Additionally,

as illustrated in this study, the retrieval can be used to study the representation of ice hydrometeors in radiative transfer simulations, which will be vital to many applications of observations from upcoming sub-millimeter sensors such as ICI and the Arctic Weather Satellite (ESA, 2021).

Appendix A

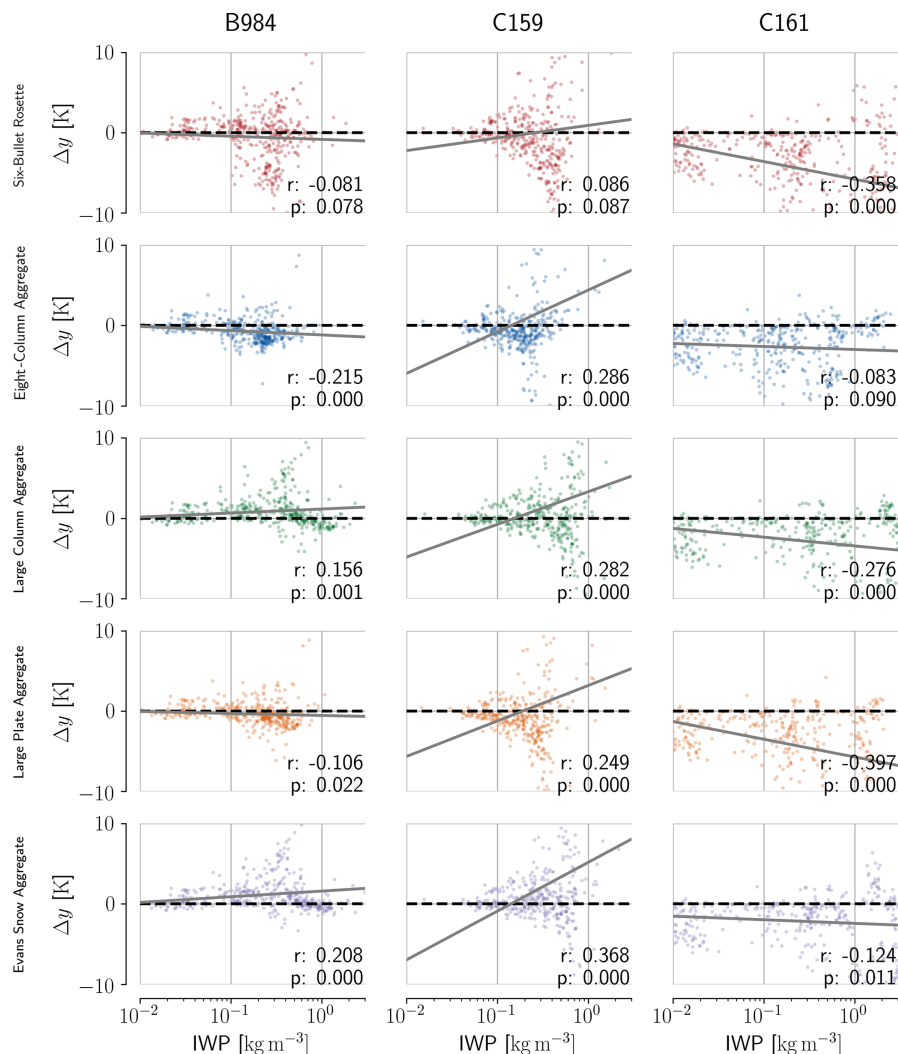


Figure A1. Scatter plots of retrieved IWP and corresponding residual in the fitted observations for the 325 ± 3.5 GHz ISMAR channel. Each column displays the residual distributions for the five different particle habits. The grey line in each panel represents the regression line for the plotted data points. The text displays the correlation coefficient r and the p value of a two-sided significance test for the slope of regression line.

Code availability. All code used to produce the results in this study is available through public repositories (<https://doi.org/10.5281/zenodo.3467316>, Pfreundschuh, 2019; <https://doi.org/10.5281/zenodo.5537885>, Pfreundschuh, 2021).

Data availability. A detailed listing of the datasets that were used in this study together with their sources is provided in Table 1. Hersbach et al. (2018) was downloaded from the Copernicus Climate Change Service (C3S) Climate Data Store (<https://doi.org/10.24381/cds.adbb2d47>).

Author contributions. SP performed the retrieval calculations and data analysis as well as writing the paper. PE, SAB, MB, DD and SP collaborated on the study that lead to the development of the presented algorithm. SF, RC and FE provided the flight campaign data and guidance regarding their usage and contributed to the interpretation and discussion of the retrieval results.

Competing interests. At least one of the (co-)authors is a member of the editorial board of *Atmospheric Measurement Techniques*. The peer-review process was guided by an independent editor, and the authors have also no other competing interests to declare.

Disclaimer. The results contain modified Copernicus Climate Change Service information 2021. Neither the European Commission nor ECMWF is responsible for any use that may be made of the Copernicus information or data it contains.

Publisher's note: Copernicus Publications remains neutral with regard to jurisdictional claims in published maps and institutional affiliations.

Acknowledgements. The work of Simon Pfreundschuh and Patrick Eriksson on this study was financially supported by the Swedish National Space Agency (SNSA) under grants 150/14 and 166/18.

Stefan A. Buehler was supported by the Deutsche Forschungsgemeinschaft (DFG, German Research Foundation) under Germany's Excellence Strategy – EXC 2037 “Climate, Climatic Change, and Society” – Project Number: 390683824, contributing to the Center for Earth System Research and Sustainability (CEN) of Universität Hamburg.

Stefan A. Buehler's work contributes to the Cluster of Excellence “CLICCS – Climate, Climatic Change, and Society” funded by the Deutsche Forschungsgemeinschaft DFG (EXC 2037, Project Number 390683824), and to the Center for Earth System Research and Sustainability (CEN) of Universität Hamburg.

The computations for this study were performed using several freely available programming languages and software packages, most prominently the Python language (The Python Language Foundation, 2018); the IPython computing environment (Perez and Granger, 2007); the numpy (van der Walt et al., 2011), pandas (Reback et al., 2021) and xarray (Hoyer and Hamman, 2017) packages for numerical computing; the satpy package (Raspaud et al., 2021) for the processing of satellite data; and matplotlib for generating figures (Hunter, 2007).

The computations were performed on resources at Chalmers Centre for Computational Science and Engineering (C3SE) provided by the Swedish National Infrastructure for Computing (SNIC).

HALO data are from SPP 1294 “High Altitude and Long Range Research Aircraft (HALO)”, funded by the German Research Foundation (Deutsche Forschungsgemeinschaft – DFG), project number 316646266.

The FAAM BAe-146 research aircraft is operated by Airtask and Avalon and managed by the Facility for Airborne Atmospheric Measurements. The flights used for this study were funded by the Met Office and European Space Agency.

Financial support. This research has been supported by the Swedish National Space Agency (grant nos. 150/14 and 166/18), the Deutsche Forschungsgemeinschaft (DFG, German Research Foundation; EXC 2037 “Climate, Climatic Change, and Society” – project nos. 390683824 and 316646266), the Met Office and European Space Agency.

Review statement. This paper was edited by Gianfranco Vulpiani and reviewed by three anonymous referees.

References

- Barlakas, V. and Eriksson, P.: Three Dimensional Radiative Effects in Passive Millimeter/Sub-Millimeter All-sky Observations, *Remote Sens.*, 12, 531, <https://doi.org/10.3390/rs12030531>, 2020.
- Barlakas, V., Geer, A. J., and Eriksson, P.: Introducing hydrometeor orientation into all-sky microwave and submillimeter assimilation, *Atmos. Meas. Tech.*, 14, 3427–3447, <https://doi.org/10.5194/amt-14-3427-2021>, 2021.
- Battaglia, A., Tanelli, S., Kobayashi, S., Zrníc, D., Hogan, R. J., and Simmer, C.: Multiple-scattering in radar systems: A review, *J. Quant. Spectrosc. Ra.*, 111, 917–947, 2010.
- Buehler, S. A., Defer, E., Evans, F., Eliasson, S., Mendrok, J., Eriksson, P., Lee, C., Jiménez, C., Prigent, C., Crewell, S., Kasai, Y., Bennartz, R., and Gasiewski, A. J.: Observing ice clouds in the submillimeter spectral range: the CloudIce mission proposal for ESA's Earth Explorer 8, *Atmos. Meas. Tech.*, 5, 1529–1549, <https://doi.org/10.5194/amt-5-1529-2012>, 2012.
- Buehler, S. A., Mendrok, J., Eriksson, P., Perrin, A., Larsson, R., and Lemke, O.: ARTS, the Atmospheric Radiative Transfer Simulator – version 2.2, the planetary toolbox edition, *Geosci. Model Dev.*, 11, 1537–1556, <https://doi.org/10.5194/gmd-11-1537-2018>, 2018.
- Cady-Pereira, K., Alvarado, M., Mlawer, E., Iacono, M., Delamere, J., and Pernak, R.: AER Line File Parameters (v3.8.1), Zenodo [data set], <https://doi.org/10.5281/zenodo.5120012>, 2020.
- Cazenave, Q., Ceccaldi, M., Delanoë, J., Pelon, J., Groß, S., and Heymsfield, A.: Evolution of DARDAR-CLOUD ice cloud retrievals: new parameters and impacts on the retrieved microphysical properties, *Atmos. Meas. Tech.*, 12, 2819–2835, <https://doi.org/10.5194/amt-12-2819-2019>, 2019.
- CloudSat DPC: 1B-CPR, CloudSat DPC [data set], available at: <https://www.cloudsat.cira.colostate.edu/data-products/1b-cpr> (last access: 1 February 2022), 2021.
- Delanoë, J., Protat, A., Testud, J., Bouniol, D., Heymsfield, A. J., Bansemer, A., Brown, P., and Forbes, R.: Statistical properties of the normalized ice particle size distribution, *J. Geophys. Res.-Atmos.*, 110, D10201, <https://doi.org/10.1029/2004JD005405>, 2005.
- Duncan, D. I. and Eriksson, P.: An update on global atmospheric ice estimates from satellite observations and reanalyses, *Atmos. Chem. Phys.*, 18, 11205–11219, <https://doi.org/10.5194/acp-18-11205-2018>, 2018.
- Eliasson, S., Buehler, S. A., Milz, M., Eriksson, P., and John, V. O.: Assessing observed and modelled spatial distributions of ice water path using satellite data, *Atmos. Chem. Phys.*, 11, 375–391, <https://doi.org/10.5194/acp-11-375-2011>, 2011.
- Eriksson, P., Ekström, M., Rydberg, B., and Murtagh, D. P.: First Odin sub-mm retrievals in the tropical upper troposphere: ice cloud properties, *Atmos. Chem. Phys.*, 7, 471–483, <https://doi.org/10.5194/acp-7-471-2007>, 2007.
- Eriksson, P., Ekelund, R., Mendrok, J., Brath, M., Lemke, O., and Buehler, S. A.: A general database of hydrometeor single scattering properties at microwave and submillimetre wavelengths, *Earth Syst. Sci. Data*, 10, 1301–1326, <https://doi.org/10.5194/essd-10-1301-2018>, 2018.
- Eriksson, P., Rydberg, B., Mattioli, V., Thoss, A., Accadia, C., Klein, U., and Buehler, S. A.: Towards an operational Ice Cloud Imager (ICI) retrieval product, *Atmos. Meas. Tech.*, 13, 53–71, <https://doi.org/10.5194/amt-13-53-2020>, 2020.

- ESA: ESA – Arctic Weather Satellite, available at: https://www.esa.int/Applications/Observing_the_Earth/Meteorological_missions/Arctic_Weather_Satellite, last access: 27 September 2021.
- Evans, K. F., Walter, S. J., Heymsfield, A. J., and Deeter, M. N.: Modeling of Submillimeter Passive Remote Sensing of Cirrus Clouds, *J. Appl. Meteorol.*, 37, 184–205, [https://doi.org/10.1175/1520-0450\(1998\)037<0184:MOSPRS>2.0.CO;2](https://doi.org/10.1175/1520-0450(1998)037<0184:MOSPRS>2.0.CO;2), 1998.
- Evans, K. F., Wang, J. R., Racette, P. E., Heymsfield, G., and Li, L.: Ice Cloud Retrievals and Analysis with the Compact Scanning Submillimeter Imaging Radiometer and the Cloud Radar System during CRYSTAL FACE, *J. Appl. Meteorol.*, 44, 839–859, <https://doi.org/10.1175/JAM2250.1>, 2005.
- Ewald, F., Groß, S., Hagen, M., Hirsch, L., Delanoë, J., and Bauer-Pfundstein, M.: Calibration of a 35 GHz airborne cloud radar: lessons learned and intercomparisons with 94 GHz cloud radars, *Atmos. Meas. Tech.*, 12, 1815–1839, <https://doi.org/10.5194/amt-12-1815-2019>, 2019.
- Ewald, F., Groß, S., Wirth, M., Delanoë, J., Fox, S., and Mayer, B.: Why we need radar, lidar, and solar radiance observations to constrain ice cloud microphysics, *Atmos. Meas. Tech.*, 14, 5029–5047, <https://doi.org/10.5194/amt-14-5029-2021>, 2021.
- Facility for Airborne Atmospheric Measurements, Natural Environment Research Council, Met Office: FAAM B984 ISMAR and T-NAWDEX flight: Airborne atmospheric measurements from core instrument suite on board the BAE-146 aircraft, Centre for Environmental Data Analysis [data set], available at: <https://catalogue.ceda.ac.uk/uuid/46ca2a2cc8ce497fbf06beaf31f67098> (last access: 1 February 2022), 2016.
- Facility for Airborne Atmospheric Measurements, Natural Environment Research Council, Met Office: FAAM C159 PIKNMIX-F flight: Airborne atmospheric measurements from core and non-core instrument suites on board the BAE-146 aircraft, Centre for Environmental Data Analysis [data set], available at: <https://catalogue.ceda.ac.uk/uuid/68cfc7f294554646803c80b2a389e105> (last access: 1 February 2022), 2019a.
- Facility for Airborne Atmospheric Measurements, Natural Environment Research Council, Met Office: FAAM C161 PIKNMIX-F flight: Airborne atmospheric measurements from core and non-core instrument suites on board the BAE-146 aircraft, Centre for Environmental Data Analysis [data set], available at: <https://catalogue.ceda.ac.uk/uuid/133e15c47c024aa4b30e3f6f54af8b77> (last access: 1 February 2022), 2019b.
- Fox, S.: An Evaluation of Radiative Transfer Simulations of Cloudy Scenes from a Numerical Weather Prediction Model at Sub-Millimetre Frequencies Using Airborne Observations, *Remote Sens.*, 12, 2758, <https://doi.org/10.3390/rs12172758>, 2020.
- Fox, S., Lee, C., Moyna, B., Philipp, M., Rule, I., Rogers, S., King, R., Oldfield, M., Rea, S., Henry, M., Wang, H., and Harlow, R. C.: ISMAR: an airborne submillimetre radiometer, *Atmos. Meas. Tech.*, 10, 477–490, <https://doi.org/10.5194/amt-10-477-2017>, 2017.
- Geer, A. J.: Physical characteristics of frozen hydrometeors inferred with parameter estimation, *Atmos. Meas. Tech.*, 14, 5369–5395, <https://doi.org/10.5194/amt-14-5369-2021>, 2021.
- Geer, A. J., Baordo, F., Bormann, N., Chambon, P., English, S. J., Kazumori, M., Lawrence, H., Lean, P., Lonitz, K., and Lupu, C.: The growing impact of satellite observations sensitive to humidity, cloud and precipitation, *Q. J. R. Meteorol. Soc.*, 143, 3189–3206, <https://doi.org/10.1002/qj.3172>, 2017.
- Hersbach, H., Bell, B., Berrisford, P., Biavati, G., Horányi, A., Muñoz Sabater, J., Nicolas, J., Peubey, C., Radu, R., Rozum, I., Schepers, D., Simmons, A., Soci, C., Dee, D., and Thépaut, J.-N.: ERA5 hourly data on single levels from 1979 to present, Copernicus Climate Change Service (C3S) Climate Data Store (CDS) [data set], <https://doi.org/10.24381/cds.adbb2d47>, 2018.
- Hoyer, S. and Hamman, J.: xarray: N-D labeled arrays and datasets in Python, *Journal of Open Research Software*, 5, p. 10, <https://doi.org/10.5334/jors.148>, 2017.
- Hunter, J. D.: Matplotlib: A 2D graphics environment, *Comput. Sci. Eng.*, 9, 90–95, <https://doi.org/10.1109/MCSE.2007.55>, 2007.
- Konow, H., Jacob, M., Ament, F., Crewell, S., Ewald, F., Hagen, M., Hirsch, L., Jansen, F., Mech, M., and Stevens, B.: HALO Microwave Package measurements during North Atlantic Waveguide and Downstream impact EXperiment (NAWDEX), World Data Center for Climate (WDCC) at DKRZ [data set], https://doi.org/10.1594/WDCC/HALO_measurements_4, 2018.
- Korolev, A., Strapp, J. W., Isaac, G. A., and Emery, E.: Improved Airborne Hot-Wire Measurements of Ice Water Content in Clouds, *J. Appl. Opt.*, 30, 2121–2131, <https://doi.org/10.1175/JTECH-D-13-00007.1>, 2013.
- Krautstrunk, M. and Giez, A.: The transition from FALCON to HALO era airborne atmospheric research, in: *Atmospheric Physics*, Springer, 609–624, https://doi.org/10.1007/978-3-642-30183-4_37, 2012.
- McGrath, A. and Hewison, T.: Measuring the accuracy of MARSS – An airborne microwave radiometer, *J. Atmos. Ocean. Tech.*, 18, 2003–2012, 2001.
- Mech, M., Orlandi, E., Crewell, S., Ament, F., Hirsch, L., Hagen, M., Peters, G., and Stevens, B.: HAMP – the microwave package on the High Altitude and Long range research aircraft (HALO), *Atmos. Meas. Tech.*, 7, 4539–4553, <https://doi.org/10.5194/amt-7-4539-2014>, 2014.
- Mlawer, E. J., Payne, V. H., Moncet, J.-L., and Delamere, J. S., Alvarado, M. J., and Tobin, D. C.: Development and recent evaluation of the MT_CKD model of continuum absorption, *Phil. Trans. R. Soc. A*, 370, 2520–2556, 2012.
- MODIS Characterization Support Team (MCST): MODIS 1km Calibrated Radiances Product, Atmosphere Archive and Distribution System (LAADS) Distributed Active Archive Center (DAAC), National Aeronautics and Space Administration (NASA) [data set], <https://doi.org/10.5067/MODIS/MYD021KM.061>, 2017.
- O'Shea, S., Crosier, J., Dorsey, J., Gallagher, L., Schledewitz, W., Bower, K., Schlenczek, O., Bormann, S., Cotton, R., Westbrook, C., and Ulanowski, Z.: Characterising optical array particle imaging probes: implications for small-ice-crystal observations, *Atmos. Meas. Tech.*, 14, 1917–1939, <https://doi.org/10.5194/amt-14-1917-2021>, 2021.
- O'Shea, S. J., Crosier, J., Dorsey, J., Schledewitz, W., Crawford, I., Bormann, S., Cotton, R., and Bansemmer, A.: Revisiting particle sizing using greyscale optical array probes: evaluation using laboratory experiments and synthetic data, *Atmos. Meas. Tech.*, 12, 3067–3079, <https://doi.org/10.5194/amt-12-3067-2019>, 2019.

- Perez, F. and Granger, B. E.: IPython: A System for Interactive Scientific Computing, *Comput. Sci. Eng.*, 9, 21–29, <https://doi.org/10.1109/MCSE.2007.53>, 2007.
- Pfreundschuh, S.: mcrf – A microwave cloud retrieval framework, Zenodo [code], <https://doi.org/10.5281/zenodo.3467316>, 2019.
- Pfreundschuh, S.: ISMAR combined retrievals (v0.0), Zenodo [code], <https://doi.org/10.5281/zenodo.5537885>, 2021.
- Pfreundschuh, S., Eriksson, P., Buehler, S. A., Brath, M., Duncan, D., Larsson, R., and Ekelund, R.: Synergistic radar and radiometer retrievals of ice hydrometeors, *Atmos. Meas. Tech.*, 13, 4219–4245, <https://doi.org/10.5194/amt-13-4219-2020>, 2020.
- Raspaud, M., Hoese, D., Lahtinen, P., Finkensieper, S., Holl, G., Dybbroe, A., Proud, S., Meraner, A., Feltz, J., Zhang, X., Joro, S., Roberts, W., Ørum Rasmussen, L., BENR0, Méndez, J. H. B., Zhu, Y., strandgren, Daruwala, R., Jasmin, T., Kliche, C., Barnie, T., Sigurðsson, E., Garcia, R. K., Lepelt, T., TT, ColinDuff, Egede, U., LTMeyer, Itkin, M., and Goodson, R.: pytroll/satpy: Version 0.30.0, Zenodo [code], <https://doi.org/10.5281/zenodo.5514044>, 2021.
- Reback, J., jbrockmendel, McKinney, W., den Bossche, J. V., Augspurger, T., Cloud, P., Hawkins, S., gfyong, Roeschke, M., Sinhrks, Klein, A., Petersen, T., Tratner, J., She, C., Ayd, W., Hoefler, P., Naveh, S., Garcia, M., Schendel, J., Hayden, A., Saxton, D., Darbyshire, J., Shadrach, R., Gorelli, M. E., Li, F., Jancauskas, V., McMaster, A., Zeitlin, M., Battiston, P., and Seabold, S.: pandas-dev/pandas: Pandas 1.3.3, Zenodo [code], <https://doi.org/10.5281/zenodo.5501881>, 2021.
- Rodgers, C. D.: Inverse methods for atmospheric sounding: theory and practice, vol. 2, World scientific, <https://doi.org/10.1142/3171>, 2000.
- Rosenkranz, P. W.: Absorption of microwaves by atmospheric gases, in: *Atmospheric remote sensing by microwave radiometry*, edited by: Janssen, M. A., John Wiley and Sons, Inc., New York, USA, 37–90, 1993.
- Schäfler, A., Craig, G., Wernli, H., Arbogast, P., Doyle, J. D., McTaggart-Cowan, R., Methven, J., Rivière, G., Ament, F., Boettcher, M., Bramberger, M., Cazenave, Q., Cotton, R., Crewell, S., Delanoë, J., Dörnbrack, A., Ehrlich, A., Ewald, F., Fix, A., Grams, C. M., Gray, S. L., Grob, H., Groß, S., Hagen, M., Harvey, B., Hirsch, L., Jacob, M., Kölling, T., Konow, H., Lemmerz, C., Lux, O., Magnusson, L., Mayer, B., Mech, M., Moore, R., Pelon, J., Quinting, J., Rahm, S., Rapp, M., Rautenhaus, M., Reitebuch, O., Reynolds, C. A., Sodemann, H., Spengler, T., Vaughan, G., Wendisch, M., Wirth, M., Witschas, B., Wolf, K., and Zinner, T.: The North Atlantic Waveguide and Downstream Impact Experiment, *B. Am. Meteorol. Soc.*, 99, 1607–1637, <https://doi.org/10.1175/BAMS-D-17-0003.1>, 2018.
- Stamnes, K., Tsay, S.-C., Wiscombe, W., and Laszlo, I.: DISORT, a general-purpose Fortran program for discrete-ordinate-method radiative transfer in scattering and emitting layered media: documentation of methodology, Tech. rep., Tech. rep., Dept. of Physics and Engineering Physics, Stevens Institute of Technology, 2000.
- Tanelli, S., Durden, S. L., Im, E., Pak, K. S., Reinke, D. G., Partain, P., Haynes, J. M., and Marchand, R. T.: CloudSat's Cloud Profiling Radar After Two Years in Orbit: Performance, Calibration, and Processing, *IEEE T. Geosci. Remote*, 46, 3560–3573, <https://doi.org/10.1109/TGRS.2008.2002030>, 2008.
- The Python Language Foundation: The Python Language Reference, available at: <https://docs.python.org/3/reference/index.html> (last access: 1 February 2022), 2018.
- van der Walt, S., Colbert, S. C., and Varoquaux, G.: The NumPy Array: A Structure for Efficient Numerical Computation, *Comput. Sci. Eng.*, 13, 22–30, <https://doi.org/10.1109/MCSE.2011.37>, 2011.
- Waliser, D. E., Li, J.-L. F., Woods, C. P., Austin, R. T., Bacmeister, J., Chern, J., Del Genio, A., Jiang, J. H., Kuang, Z., Meng, H., Minnis, P., Platnick, S., Rossow, W. B., Stephens, G. L., Sun-Mack, S., Tao, W.-K., Tompkins, A. M., Vane, D. G., Walker, C., and Wu, D.: Cloud ice: A climate model challenge with signs and expectations of progress, *J. Geophys. Res.-Atmos.*, 114, D00A21, <https://doi.org/10.1029/2008JD010015>, 2009.
- Zelinka, M. D., Myers, T. A., McCoy, D. T., Po-Chedley, S., Caldwell, P. M., Ceppi, P., Klein, S. A., and Taylor, K. E.: Causes of Higher Climate Sensitivity in CMIP6 Models, *Geophys. Res. Lett.*, 47, e2019GL085782, <https://doi.org/10.1029/2019GL085782>, 2020.